Vilnius University
Physics Faculty
Laser Research Center

Eulàlia Puig Vilardell

Fabrication of 3D Gradient Photonic Structures via Laser Lithography and its Characterization

Master's final thesis

Laser Technologies study program

Supervisor	Prof. Mangirdas Malinauskas
Consultant	Dr. Darius Gailevičius
Reviewer	Dr. Domas Paipulas
Head of Department	Dr. Dalia Kaškelytė

Vilnius 2024

Contents

1 Introduction

Additive manufacturing techniques using light to induce polymerization of photosensitive materials [1] are well-established techniques for printing 3D structures that have been used over the last decades [2]. Among them, Laser Direct Writing techniques (LDW) have attracted a lot of attention given the ability that lasers own of confining the optical energy in a restricted small space, procuring as a result a highly accurate and controllable fabrication processing zone.

Two-Photon Lithography (TPL) [3], [4], is a LDW that allows high-precision 3D micro and nano-structures manufacturing with sub-diffraction-limit resolution. Thanks to the advent of femtosecond lasers, nonlinear light-matter interactions are achievable by focusing such high intensity beams into the photoresins, which due to temporal and spatial overlap can result in two- or even multi-photon absorption inside the volume of the tightly focused laser beam, allowing to polymerize the material in a small confined region.
This significant advantage makes it a suitable and high desirable technique for the fabrication of micro and nanoscale 3D structures, and it's been widely employed for applications in several fields such as micro-optics [5], microelectronics [3], microfluidics [6], life sciences [7], and photonics [8], to mention some of them. This project is based on one of these applications: micro-photonics, more specifically on the fabrication of 3D Photonic Crystals (PhC).

Photonic crystals on his side, are materials that have a periodic modulation of the refractive index, which has direct effects on the propagation of electromagnetic waves at the wavelength scale [9]. This property makes these materials an attractive and interesting tool to control and manipulate the flow of light, making possible phenomena that is not feasible to achieve with ordinary materials like strong light confinement, negative refraction [10], or slow light states [11]. This materials have drawn a lot of attention of both theorists and experimentalists, and are being used already in numerous applications such as in optical sensors [12], optical signal processing devices [13], filters [14] and fiber optics [15] to name a few.
Even though 3D PhC appear as the most attractive ones, owing the fact that they can intrinsically possess complete band gaps and thus allow to control the light in all dimensions, they are also the most challenging to fabricate, making 2D PhC the ones that have been exploited more for the moment being. In this work, the realization of a novel type of 3D PhC presenting slow light and spectral localization has been explored.
It's important to stress that this structured materials affect photons at the wavelength scale, meaning that the crystallographic arrangement should be on the nanometers scale. Therefore, in order to fabricate functional 3D photonic crystals, 3D nano-fabrication techniques are required, being Two-Photon Lithography one of the suitable techniques to fabricate them given that it allows the fabrication of complex 3D structures with high precision and sub-diffraction-limit resolution.

Before getting into the subject, it has to be mentioned that this work is a continuation of a project in progress that was started some years ago as a collaboration between Vilnius University (VU), Universitat Politècnica de Catalunya (UPC) and Shizuoka University. Because of that, this study is not starting from the very ground level but from an already

intermediate state, taking the knowledge acquired from the previous people working on it. During the past year, structures presenting some of the desired features were fabricated successfully, but given that a different fabrication system was used in that case, it is expected to have to make modifications in order to achieve the results with the equipment available for this work. Nonetheless, both the workflow and the structure's parameters that were used have been taken as starting point, making the characterization of the results obtained with them an important step of the process.

The goal of this study is to fabricate via TPL a 3D gradient photonic crystal able to slow down and spectrally localize the light in the near infrared regime.

The tasks set to achieve this goal are the following:

1. Fabricate via TPL the structures designed formerly in the frame of the project in collaboration with UPC and Shizuoka University and analyse them using microscopy techniques.

2. Study the influence of the fabrication parameters and optimize them in order to achieve the desired slow light and rainbow trapping effects for the near infrared regime.

3. Simulate using numerical methods relevant aspects of the PhC and its interaction with light to understand their behaviour.

4. Join modelling and characterization measurements in UPC to assess the performance of the 3D gradient structures as photonic crystals.

2 Literature Review

2.1 Photopolymerization Mechanisms

Photolithography techniques rely on the response of a photosensitive material to light, which can be additive or subtractive depending on the material's properties. In the former, the interaction with light results in the polymerization of the monomers/oligomers of the material, i.e. cross-linking of the pre-polymer's molecules, while in the latter it induces the opposite reaction, the break of polymer chains. The relevant one for the study at hand is the first, also referred to as photopolymerization techniques [16], which are actually the most popular and widely used for fabricating complex 3D structures, and which is the one used in this work.

The term photopolymerization is used to describe a polymerization reaction that is being initiated by light [17]. By absorbing one, two or multiple photons, the molecules can be excited from the singlet ground state (S0) to the excited singlet manifold (S1), and from that state undergo bond cleavage (bond breaking). There are two ways in which the covalent bonds can break: the most familiar one, in which one of the resultant molecules takes both electrons of the bond, giving as products a cation and an anion, which receives the name "heterolytic cleavage", and another, in which the bond is separated evenly, each of the resulting molecules taking one of the electrons bonding them, named "homolytic cleavage", in which case the resulting products are free radicals (molecule containing an unpaired electron in an atomic orbital). In both cases, the resultant species are highly reactive and by interacting with the monomers can induce a cross-linking reaction chain that propagates and gives place to a three-dimensional network of polymer chains.

The specific way in which the molecule dissociates and therefore the type of polymerization that takes place depend on the characteristics of the material, and for the case of the resin used in this work, an hybrid organic-inorganic photopolymer called SZ2080™, this pathway is radical polymerization: the excited molecules relax to the triplet state (T1) after being excited to the singlet state (S1) by inter-system crossing and dissociate by homolytic cleavage, giving place to free radicals that will initiate the polymerization reaction [18].

The radical photopolymerization mechanism is described in equations (1, 2, 3, 4) and can be thought of as a three stage process:

1. **Inititiation** - The photosensitive molecules are excited by the incident light, give place to an active center, and start to interact with monomers.

2. **Propagation** - The chain elongates rapidly by the interaction of free bonds with unreacted monomers.

3. **Termination** - A molecule that attaches to the free bond of the chain gives as a product an un-reactive specimen, as for example happens when the free bond reacts with a free radical, another polymer chain with a free bond, or even to oxygen molecules, or when two closed non-reactive chains result from an hydrogen being torn apart from one chain and attached to another chain.

Initiation

$$\text{Bond cleavage:} \quad PS+ \xrightarrow{h\nu} R^* \tag{1}$$

$$\text{Initiation:} \quad R^* + M_1 \rightarrow RM_1^* \tag{2}$$

Propagation

$$\text{Propagation:} \quad RM_1^* + M_2 \rightarrow RM_1M_2^*$$
$$RM_1...M_n^* + M_m \rightarrow RM_{n+m}^* \tag{3}$$

Termination

$$\text{Recombination:} \quad RM_l^* + RM_k^* \rightarrow RM_{l+k}R$$
$$RM_l^* + R* \rightarrow RM_lR \tag{4}$$

$$\text{Disproportionation:} \quad M_l^* + HM_k^* \rightarrow HM_l + M_k \tag{5}$$

$$\text{Inhibition:} \quad RM_l^* + O_2 \rightarrow RM_lOO \tag{6}$$

being PS a Photosensitive molecule, R^* a free radical, M the monomers, and H and O hydrogen and oxygen atoms correspondingly [18].

At this point it has to be mentioned that a modification of the equations has been introduced to adapt them to a more general situation, which includes the particular case of this study. In literature it has only been found as starting specie the acronym PI, standing for "Photoinitiator", instead of PS, "Photosensitive". Most of the times, the pre-polymer consist of a mixture of monomers/oligomers and a photoinitiator, which is a material with low photodissociation energy that is used to enhance the photosensitivity of the material and increase the efficiency of the polymerization. Nevertheless, it has been proven that for some materials, photopolymerization is also achievable without the presence of a photoinitiator [19], being the case of SZ2080™, for which it has been also shown that the use of the non-photosensitized material might be even preferable due to a higher resilience, i.e. higher laser induced damage threshold [20], and higher resolution [19]. Because of that, and considering as well that photoinitiators are in general toxic compounds, and light absorbing molecules that remain present in the resin [21] and may induce some undesirable absorption after fabrication is finished, non-photosensitized SZ2080™ has been used for this study.

2.1.1 Two-Photon Lithography

TPL is a nonlinear photopolymerization technique that can work both as an additive or a subtractive manufacturing technique [22]. The whole process consists in the following steps: design, sample preparation, fabrication, chemical development and characterization, which sometimes is not included as part of the steps, but it's actually of high importance given that this is a complex technique in which a lot of factors can have an impact on the final result, reason why it's key to check the outcome, and depending on it, make modifications on some of the steps in order to achieve the desired result.

The resins employed as pre-polymer/photosensitive resins are designed to be sensitive to UV but transparent to most visible and NIR radiation ($\lambda_0 > 400$nm) [23]. This means that radiation of longer wavelengths will not be absorbed for the resin unless it's focused tightly enough so that the light's spatio-temporal localization allows multi-photon absorption to take place. This process can be described as the excitation of an electron from one state to another of higher energy by the simultaneously absorption of n photons of energy $E_{1\to2}/n$ ($E_1 < E_2$) as represented in 1, each of them exciting the electron to an intermediate virtual state, and the next absorbed photon being absorbed within the virtual state life time, which is of the order of femtoseconds, reason why ultrafast lasers of high intensity are employed in this technique.

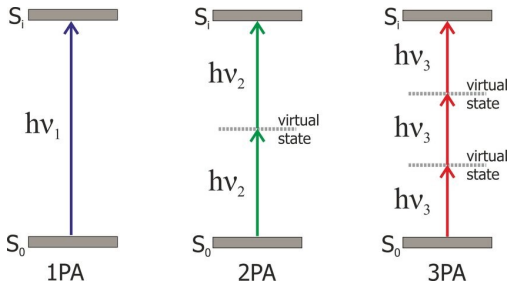

Figure 1: One-, two-, three-, and four-photon absorption energy levels diagram, reproduced from [24].

When focusing the laser beam with a high NA lens, the beam propagates through the resin without interacting with it except in the limited volume where it's focused, place in which the previous condition is satisfied. This allows to induce polarization in a small localized volume inside the resin, and by scanning it (or moving the stages), it allows to create 3D structures that will reproduce the path followed by the laser. Nevertheless, a sufficient degree of cross-linking should be achieved for the resin to experience a permanent transformation, which otherwise will be washed away when developing it in the solvent.

The smallest element, i.e. volumetric pixel, commonly referred to as 'voxel', and the resolution that can be achieved, are defined by physical, chemical and engineering thresholds, as well as on the material response (sensitivity and diffusion of reaction), and undeniably on the exposure parameters (intensity, I [W/cm^2] and energy dose, D [J]). A relevant concept regarding this is the idea of "polymerization window", which is the ratio between the intensity at which polymer damage occurs I_{odt}, and the intensity at which the polymerization reaction starts to take place $I_{pt} = (I_{odt} - I_{pt})/I_{pt}$, that gives an idea of how big is the range of optimal intensities for structure fabrication [18].

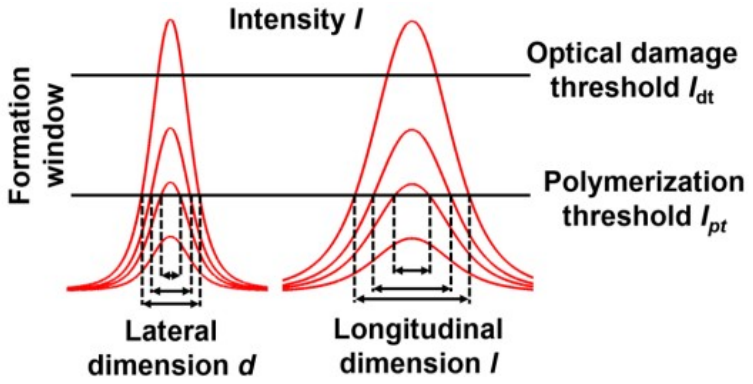

Figure 2: Dependence of the dimensions of the polymerized segment (voxel) on the intensity of the exposed laser beam in the focal plane and the thresholds of polymerization and polymer optical damage. [25]

As it can be observed in Fig. 2, by exposing the resin with only the top of the gaussian beam intensity, it is possible to achieve the smallest feature's dimensions and the highest resolution. The intensity can be calculated from the average power through:

$$I = \frac{2PT}{fw^2\pi\tau} \tag{7}$$

where P is the average laser power, T the transmission of the objective, f the repetition rate, w the beam waist radius and τ the pulse duration.

The dimensions of the voxels as well as the degree of cross-linking will not only be determined by the intensity, which sets a threshold for nonlinear absorption and thus photopolymerization, but also by the exposure dose. Taking into consideration that the pulses of the lasers used in this technique have pulse durations of the order of femtoseconds and repetition rates of at least hundreds of kilohertz, the amount of pulses affecting a single segment of the material, i.e. pulse overlapping, is of the order of thousands of pulses, meaning that the velocity at which the laser beam is scanned [25] will play also be an important factor, which are the reason why typically the parameters that are modified in the experiments to achieve the desired feature sizes and degree of cross-linking, are the average laser power P, and the scanning velocity v.

Lastly, it's important to mention that the formation of bonds between the resin's monomers results in a closer inter-molecular spacing, which is manifested macroscopically as a volume shrinkage of the polymerized material [26], having an impact on the features dimensions and being a cause of mechanical deformations. It's a complex process in which a lot of variables play a role: material composition, sample geometry, light irradiation, degree of external constraint, etc. and even though it's for now out of the scope of this work to study the intricate mechanisms of this process, it's necessary to take it into account given that it will influence the final result of the fabrication.

2.2 Photonic Crystals

Photonic crystals are defined in literature as high-index-contrast periodic structures [27–29]. This periodic modulation affects the propagation of light similar to how a natural crystal lattice affects the conductivity of electrons in solid state crystals, which is why sometimes photonic crystals are referred to as the optical analogue of solid state crystals. In fact, most of the concepts including the notation and nomenclature have been taken from solid-state research, where quantum mechanics were already providing an explanation for the behaviour of electrons within solids that was accepted for the scientific community.

The term "Photonic Crystal" was first mentioned in 1989 by E. Yablonovitch [30], even though in some literature [28, 29, 31, 32] it can be found that the concept was first introduced in 1987 by E. Yablonovitch [9], and John [33], where the authors discuss about this type of structures but without giving it the specific name for which they are known today. Actually regarding the name, there is a bit of controversy as whether "Photonic Crystal" should be applied to any periodic structures or just to 2D and 3D designs. Yablonovitch rejected applying it to one-dimensional band-gap structures and even wrote an article "Photonic Crystals: What's in a Name" [27] some years after he used it for the first time. In it, it's stressed that the new term was invented to fulfill the need of naming a novel type of structures, which even though were showing a similar effect (i.e. photonic band-gaps), had different requirements compared to the already known layered materials that had been explored for a long time since the idea was presented by Lord Rayleigh in 1887 [34], thus making no sense to rename structures showing one-dimensional band-gap, and reserve the name for the new structures presenting two- and three-dimensional band-gaps. In other words, or to sum up, the name "Photonic Crystal" refers to a material which apart from having a periodic index modulation, also needs to have a high index contrast (condition which is not a necessity in the 1D case).

2.2.1 Real and Reciprocal Space

As in solid-state physics, the study of the properties of the PhC is mainly done in the reciprocal space, which is essentially the Fourier transform of the real space, being the latter the physical space where atoms (solid-state physics) or periodic dielectric media (photonics) are arranged in a lattice, and the former, the mathematical space in which the spatial frequencies associated with those periodic arrangements are described.

Crystals are usually described mathematically in the real space by a lattice, a set of points reproducing the same periodicity and symmetries. The lattice is defined by a set of vectors that describe the translations needed to reproduce this pattern throughout space. For a 3D crystal, i.e. a structure periodic in all three dimensions, 3 vectors are needed for that $\{\mathbf{a}_1, \mathbf{a}_2, \mathbf{a}_3\}$. Any vector $\mathbf{R}$ resulting from a linear combination of the lattice vectors $\mathbf{R} = l\mathbf{a}_1 + m\mathbf{a}_2 + n\mathbf{a}_3$ describes a translation to a point of the lattice, and there can exist different combinations of vectors that successfully span the lattice.
Each set of vectors defines a unit cell, a repeating unit that serves as the building block of the lattice. There are different types of unit cell, body-centered unit cells (containing one

lattice point at the center of the cell), face-centered unit cells (containing lattice points at the center of each face of the cell), and a type of unit cell that deserves a special mention, the so-called primitive unit cell, which are those cells containing just one lattice point, being the smallest repeating unit that completely describes the crystal lattice and captures the essential symmetry, that is the type of unit cell that will be used for the simulations in which the dispersion relation is analysed.

Whereas in the real space we can use a lattice to describes the periodic structure, in the reciprocal space, there exists a reciprocal lattice that describes its spatial frequencies, which determines how the periodic structure interacts with waves.
The reciprocal lattice is also defined by a set of vectors $\{\mathbf{b}_1,\ \mathbf{b}_2,\ \mathbf{b}_3\}$, and as in the real lattice, any vector $\mathbf{K}$ resulting from a linear combination of the reciprocal lattice vectors $\mathbf{K} = u\mathbf{b}_1 + v\mathbf{b}_2 + w\mathbf{b}_3$ describes another point of the reciprocal lattice, i.e. another spatial frequency of the structure.

Reciprocal lattice vectors, $\mathbf{K}$, satisfy:

$$e^{i\mathbf{R}\cdot\mathbf{K}} = 1, \qquad \mathbf{R}\cdot\mathbf{K} = 2\pi n \tag{8}$$

and it's possible to construct the reciprocal lattice vectors from the real lattice vectors using the following expressions:

$$\mathbf{b}_1 = 2\pi\frac{\mathbf{a}_2\times\mathbf{a}_3}{\mathbf{a}_1\cdot(\mathbf{a}_2\times\mathbf{a}_3)} \qquad \mathbf{b}_2 = 2\pi\frac{\mathbf{a}_3\times\mathbf{a}_1}{\mathbf{a}_1\cdot(\mathbf{a}_2\times\mathbf{a}_3)} \qquad \mathbf{b}_3 = 2\pi\frac{\mathbf{a}_1\times\mathbf{a}_2}{\mathbf{a}_1\cdot(\mathbf{a}_2\times\mathbf{a}_3)} \tag{9}$$

As in the case of the real lattice, reciprocal lattice vectors can also be used to describe the cells that span the lattice, but in this case, the cell which is the most interesting to consider is the 1st Brillouin Zone (1BZ), which is the region in the reciprocal space centered in a lattice point, in which all the points are closer to that lattice point than to any of the other lattice points.

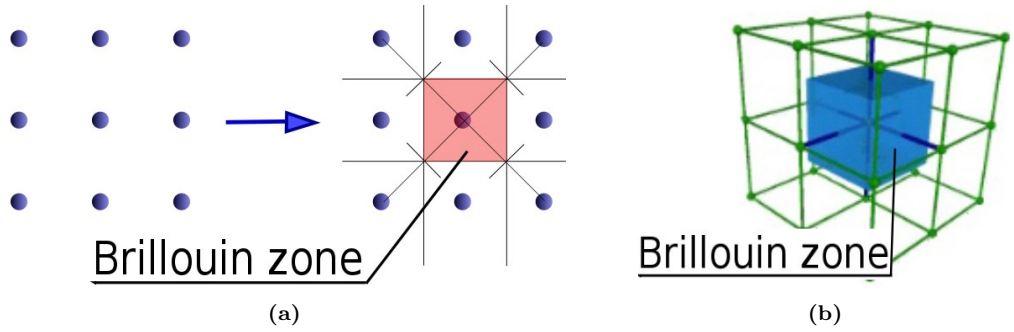

Figure 3: 1st Brillouin zone of a (a) 2D square reciprocal lattice (b) 3D cubic reciprocal lattice.

If the crystal possesses additional symmetries, the 1BZ can be redundant. In that case, it's interesting to define an even more constricted region by eliminating those redundant parts, which receives the name of irreducible Brillouin zone. This zone is the one used for the study of the dispersion relation of the structure, and the corners of the irreducible

Brillouin zone are used to scan the reciprocal space in order to identify the band gaps, given that almost all the band extrema almost occur along the boundaries of the irreducible Brillouin zone.

2.2.2 Bloch Theorem and Dispersion Relation

Research on wave propagation through three-dimensional periodic potentials was initiated by Bloch in 1928, who demonstrated that waves (electrons) can propagate without scattering in this type of potentials (crystal lattice potential), being their behaviour governed by a plane wave modulated by a periodic function of the crystal's lattice periodicity $u(\mathbf{r}) = u(\mathbf{r} + \mathbf{R})$, named Bloch wave, $\Psi(\mathbf{r}) = e^{i\mathbf{k}\cdot\mathbf{r}}u(\mathbf{r})$, which is an eigensolution to a periodic potential system's eigenproblem (Schrodinger equation)[35].

This can also be applied to electromagnetic waves, for which the system can also be described as an eigenproblem of eigenvalue (ω/c), Eq. (10), or simply ω given that c is a constant. This eigenequation can be obtained by combining Maxwell's equations and considering a time dependence e^{-iwt}, i.e. a fixed frequency ω:

$$\nabla \times \frac{1}{\varepsilon(\mathbf{r})}\nabla \times \mathbf{H}(\mathbf{r}) = \left(\frac{\omega}{c}\right)^2 \mathbf{H}(\mathbf{r}) \tag{10}$$

being $\varepsilon = \varepsilon(x, y, z)$ the dielectric function, c the speed of light, $\mathbf{H}$ the magnetic field.

Photonic crystals are, by definition, materials with a periodic dielectric function $\varepsilon(\mathbf{r}) = \varepsilon(\mathbf{r} + \mathbf{b}_i)$ where $\mathbf{b}_i$ are the primitive lattice vectors.
Solutions can be chosen of the form $\mathbf{H}(\mathbf{r}) = e^{i\mathbf{k}\cdot\mathbf{r}}\mathbf{H}_{n,\mathbf{k}}(\mathbf{r})$ by applying Bloch's theorem to Eq. (10), where $\mathbf{k}$ is a Bloch's wavevector within the 1st Brillouin zone (1BZ) and $\mathbf{H}_{n,\mathbf{k}}$ the periodic envelope function, which is labelled with two subindexes: $\mathbf{k}$ is needed because each wavevector leads to a particular eigenequation, and n is used to identify the specific discrete solutions, thus taking whole and positive values $n = 1, 2, \cdots$, [35]. The eigenvalues are also labelled in such a way that they're completely specified $\omega_n(\mathbf{k})$, but in this case it's more interesting to write them as a variable of the wavevector, being the eigenvalues a continuous function of $\mathbf{k}$ that give place to the so-called band/dispersion diagrams when plotting it, as presented in Fig. 4, mapping all possible waves that can propagate inside the crystal.

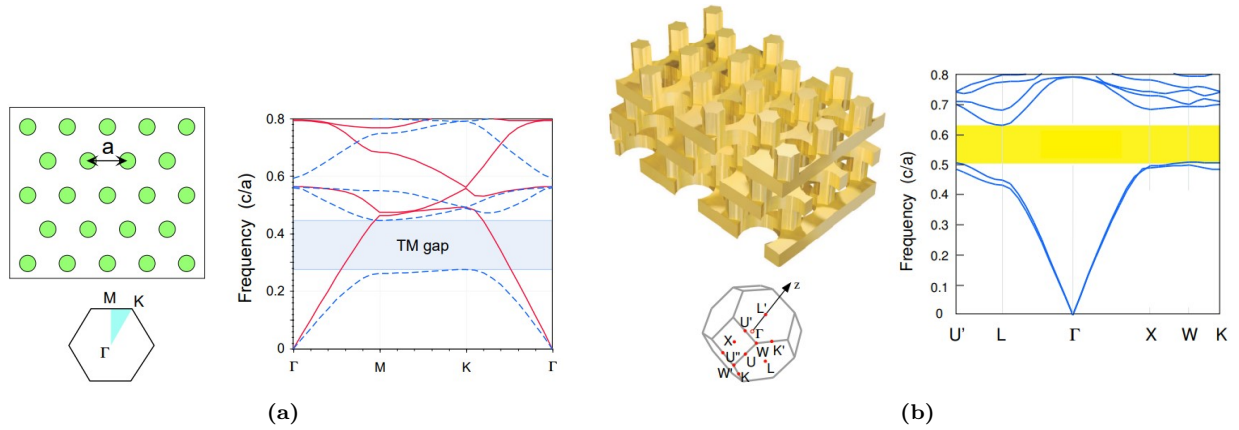

Figure 4: Photonic crystals with their respective band diagrams (a) 2D, (b) 3D. [35]

Each discrete band corresponds to an specific n, and it can happen that for a given ω there aren't any $\mathbf{k}$, in other words, no solution to the eigenproblem (propagating solution, i.e. with real wavevector $\mathbf{k}$) exists with that frequency, which can be seen in the diagram as a gap between bands, thus its naming "band-gap". Nontheless, it's common to find in literature ([32, 36, 37]) the term "complete (or full) band-gap" to refer to these cases, and use "band-gap" as a more general concept which can apply to the forbidden propagation of certain electromagnetic waves depending on the angles of incidence, i.e. when a gap arises between bands just for $\mathbf{k}$ inside some range (or an specific value).

Achieve a complete band-gap is not an easy task given that the gaps in all different directions must overlap. It's usually required to use a high index contrast material given that the higher that quantity is, the larger the band gaps are going to be, leaving thus more room for the band-gaps to overlap. Besides that, it also helps to use lattices of high symmetry, corresponding to more spherical 1BZ (or circular in 2D), which make easier the creation of a complete band-gap (the periodicity appears almost the same no matter the direction, giving place to almost identical band-gaps which will quickly overlap), [35, 36].

2.2.3 Velocity of Propagation

The phase velocity, usually given by $\omega\mathbf{k}/|\mathbf{k}|^2$, is difficult to define in photonic crystals given that the wave vector $\mathbf{k}$ is not unique and also there is a periodic envelope function $\mathbf{H}_{n,\mathbf{k}}$ modulating the plane wave (which makes it hard to identify unique phase fronts).
Instead, in periodic mediums, the direction and speed with which the electromagnetic energy passes through them are given by the group velocity $\mathbf{v}_n(\mathbf{k})$, a function of both the band index n and the wave vector $\mathbf{k}$ which corresponds to the energy-transport velocity.

$$\mathbf{v}_n(\mathbf{k}) = \nabla_k \omega_n = \frac{\partial \omega_n}{\partial k_x}\hat{x} + \frac{\partial \omega_n}{\partial k_y}\hat{y} + \frac{\partial \omega_n}{\partial k_z}\hat{z} \tag{11}$$

This can be demonstrated by obtaining an expression for the group velocity by differentiating the eigenequation on $\mathbf{H}_{n,\mathbf{k}}$ with respect to $\mathbf{k}$ and taking the inner product with $\mathbf{H}_{n,\mathbf{k}}$ on both sides. By re-arranging the terms, the final result is that $\mathbf{v}_n$ is equal to the ratio of the

energy flux to the energy density, which by definition is the velocity of energy propagation.

Considering this, the velocity at which the light will propagate through the photonic crystal can be inferred from the band diagrams, being the regions in which the curves flatten, $\nabla_k \omega_n \sim 0$, the ones corresponding to slow propagating waves, i.e. slow light.

2.2.4 Woodpile Structure

One of the types of three-dimensional photonic crystal that appear to be most effective is the woodpile structure [38], which is presented in Fig. 5a: a set of staggered layers, each one composed of an array of rods oriented in the same direction and separated a distance a, "lattice constant", perpendicular to the rods in the layer below, located at a vertical distance $c/4$, in which the rods are separated between them a distance b. Additionally, the succeeding layer with the same orientation is displaced by half the lattice constant, $a/2(b/2)$, as it's illustrated with the colors in the Fig. 5.

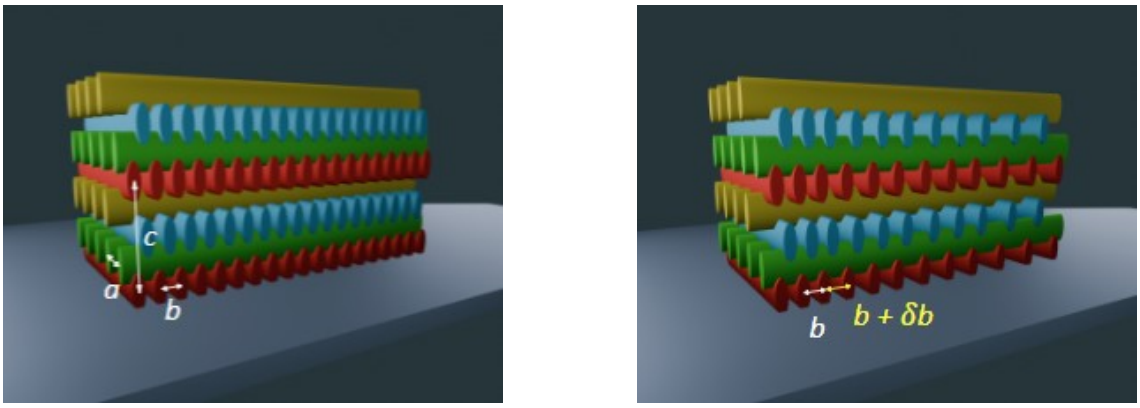

(a) **(b)**

Figure 5: Scheme of a woodpile structure (a) with orthorhombic body centered symmetry. (b) modified orthorhombic body centered symmetry woodpile with a chirp along the propagation direction.

This structure (Fig. 5a) has one of the strongest EM interactions, and given that these symmetries present some of the most spherical 1BZ, this architecture can lead to full solid photonic band gaps.

For this study, a slightly modified version of this structure has been used (Fig. 5b), in which a gradual variation on the lattice constant (periodicity) along the propagation direction is introduced. The goal of the work is not to simply achieve a band-gap, but to slow down and eventually stop the light of a broadband, providing of a region in space where the intensity is maximal. By introducing a chirp in the lattice periodicity, the dispersion relation $\omega(\mathbf{k})$ will vary along this direction, giving place to a local dispersion relation and thus, a smoothly varying local band-gap. As a consequence, the incoming radiation will gradually approach the band-gap and experience a decrease on the propagation velocity (slow down) until it reaches it, situation in which it will momentarily stop (temporary localization) and then be reflected back. But not only this, different frequencies will encounter the band-gap

at a different position (i.e. for a different lattice period), therefore stopping at a different position, giving place to the so-called rainbow trapping effect (separation of frequency components in space of slow light).
This effect has been theoretically demonstrated and experimentally shown for microwave regime, [39], and the goal of this project is to scale it down to the near infrared, which to our knowledge has not been yet experimentally realised with 3D PhC.

3 Experimental Methods

3.1 General Workflow

3.1.1 Sample Preparation

The resin used for the fabrication of the structures is the hybrid organic-inorganic photopolymer SZ2080™ , and a glass cover slip is used as substrate.

The common procedure is to drop-cast with a pipette a drop of the pre-polymer on the center of the cover slip and then heat the sample in an oven to solidify it and evaporate the solvent present.
Nevertheless, an intermediate step is done before that. The reason is that the assessment of the PhC's properties is done by measuring the light scattered by the sample, and this can be more efficiently done if the structure is as close to the substrate's edge as possible, so to be able to focus as much light as possible inside. The problem there is that the fabrication can not be directly done in the edge of the cover slip because when drop-casting the pre-polymer at an edge, the height of the material deposited is insufficient to ensure enough space inside of it to fabricate the structure. For this reason, an scratch line is engraved in the center of the cover slip with an engraving pen, which allows to split/break the cover slip into two in a controlled way after fabrication is completed. This allows to follow the common procedure of drop-casting the pre-polymer at the center of the cover slip (now on top/covering the scratch) so fabrication can be done in a place where the resin's tallness is enough, while having the control of how close to the edge (future edge, for the time being just a simple scratch) the structure is being fabricated.
After the scratch is inscribed in the glass substrate, a drop of SZ2080™ is dropped on its center (on top of the line), and then the sample is heated in a hot plate at 50^{o} for 24h. Once this procedure is done, the sample is ready for the next stage, the photopolymerization/ creation of the structure under the exposition of a laser beam.

3.1.2 Laser Direct Writing

The system used for the Laser Direct Writing process is the Laser Nanofactory System provided by Femtika, a fabrication station designed for this purpose. The system consists of a femtosecond pulsed laser source of central frequency $\lambda_c = 1035 \pm 10$ nm, pulse duration $\tau < 100$ fs, repetition rate $f = 76 \pm 0.5$ MHz, a maximum average power at the first harmonic of $P_{max} = 4$ W, and a quality beam factor $M^2 < 1.2$. It also allows to fabricate using the second harmonic $\lambda_{SH} = 517 \pm 10$ nm, which is the option chosen for this experiment.

There are two positioning stages: XYZ for the translation of the sample, which have an accuracy of ±300 nm in XY axis and ±270 nm in Z axis with maximum speed of 350 mm/s and 200 mm/s respectively, and AB for the laser beam positioning, with accuracy of 50 µrad Finally, to focus the beam onto the sample, a Plan Apochromat Zeis 63x immersion oil objective lens of 1.4 NA and transmittance $T = 0.88$ for $\lambda_0 = 517$ nm is used, allowing to tightly focus the laser beam inside the volume of the resin.

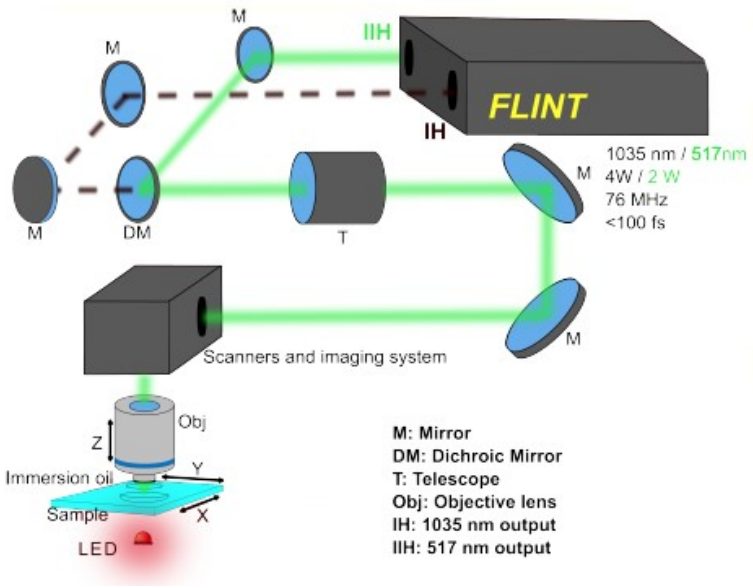

Figure 6: Simplified Laser Nanofactory System optical setup, reproduced from [40].

The Laser Nanofactory System is controlled by a software designed for this specific purpose provided by Femtika, which is divided into two applications: 3DPoli Compiler and 3DPoli Fabrication. The former is used to define the structures, i.e. the motion profiles, while the latter performs the structure fabrication from the compiled data provided by the first. The structures are defined using an internal programming language that allows to control several parameters: the position of stages (both the sample translation (X, Y, Z) and laser beam positioning (A, B)), the attenuator axis (P), the power (W, calibrated attenuator axis), the movement velocities, the opening/closing of the shutter, as well as it allows to define variables, functions, procedures, etc. A part from the tab/window to write the code, the 3DPoli Compiler application also comes with a 3D preview window in which the structure can be visualized after the code is written and compiled, and an additional window, "Structure Information" tab, in which the most important geometrical properties can be checked.

To proceed with the fabrication, the sample is placed in the sample holder with the face of the cover slip where the resin is facing down (polymer drop-down configuration), and a drop of immersion oil is placed on the top of the cover slip. The XY axes of the positioning stage are moved in order to center the sample right below the objective, and the objective is lowered by controlling the Z axis until the focal point is located in the substrate-polymer interface. Then, the translation of the XY axes is used again to find a good location for the

fabrication of the structure, which means finding where the scratch is, and define the origin for the fabrication at a reasonable distance so that the whole structure is fabricated close to but not over the scratch, so that it remains intact after the cover slip is split/broken into two.
Once the stages are set in the desired position, the code is compiled, sent for fabrication, and executed. After the program/fabrication is completed, the sample can be removed from the holder and proceed with the next stage.

3.1.3 Development Procedure

The standard procedure to develop the samples consists of immersing them in a solvent in order to wash off the parts of the resin that are not polymerized, the non-exposed regions in this case given that a negative-tone resin is being used, leaving only the 3D polymerized structure. Therefore, it is important that a sufficient degree of cross-linking is achieved during the laser exposure of the regions of interest, as equally important is to ensure that the structure polymerized is attached to the substrate (fabricated in contact with), and that the developing solvent and the time during which the sample is immersed in it is the adequate for washing off the unexposed material, but not too much to deteriorate/debilitate the polymerized structure. Development is thus a stage of the process in which, once again, a lot of parameters can influence the final result, affecting the sample in more aspects than just the intended one (leaving just the fabricated structure in the substrate) like inducing shrinkage or deformations.
For this work, the structures are develop in 4-methyl-2-pentanone for 30 minutes, after which the sample is removed from the solvent. Additional rinse is applied using a pipette and the same solvent to remove the solvent used for development which may contain residual resin's particles, and is let to dry at room temperature after.

3.1.4 Characterization

Multiple instruments are used as a first characterization of the structures, while the final spectral analysis is done in another institution with specific equipment/set-up for retrieving spectral information of the light scattered by the PhC.
It's important here to differentiate the characterization of the samples done in different stages of the study. Once the optimal parameters are found and before sending the structures for the final measurements, a simple characterization is required to assess weather the samples show evidence of being good candidates or if they present some defects and/or show signs of not performing as expected, which would result in the discard of those examples and the whole fabrication should be repeated. For this, the characterization is simply done by observing them first in an optical microscope and later in an optical scanner profilometer, which are imaging techniques that do not affect the physical (and optical) integrity of the samples and provide enough information to make the triage. On the other side, in the early stages the characterization is used to get a clear picture of the structures that are being manufactured and how slightly modifications of the printing parameters can have an influence on the resulting structures, reason why measurements that provide of additional (and relevant) information of the structures even though making them useless are included in this

phase of the work. This is the case of the Scanning Electron Microscope (SEM), which is employed in the first stages for high resolution imaging.

(a) Optical Microscope

The optical microscope Olympus BX51 is used to observe the sample both in transmission and in reflection mode, i.e. image the sample using an illumination source located in the opposite side of the stage/specimen's placement and thus observing the light that gets transmitted through, or having the illumination source in the same side as the objective and imaging it from the light that gets reflected. The magnification of the available objectives are: 4x, 10x, 20x, 40x, which even though being insufficient to resolve the details of the structures given their small dimensions, are already enough to detect big deformations or structural defects, and thus discard them in this first stage.

(b) Optical Scanning Profilometer

The LEXT™ OLS5100 3D Laser Scanning Microscope, Fig. 7a, is used to assess in more detail the structural characteristics of the printed structures, more specifically their global shape and dimensions as well as the placement and periodicity of the rods.

This microscope has two optical systems (color imaging and laser confocal) enabling to acquire color and shape information as well as high-definition images. For the current study the relevant one is the one providing shape information, i.e. the confocal imaging system. This system consists of a 405 nm laser diode as light source and a high-sensitivity photomultiplier as detector, which receives the light focused through a circular pinhole instead of all the light reflected and scattered from the sample, which helps acquiring images with higher contrast than with an ordinary microscope. The microscope automatically adjusts the focus position to capture several confocal images in order to assess height, and provides 3D shape information of the sample's surface based on the discrete focus position (Z) and detected light intensity (I) of each pixel, enabling to measure surface irregularities of the sample thanks to a shallow depth of field. The principles of the mentioned measurement are presented in Fig. 7b.

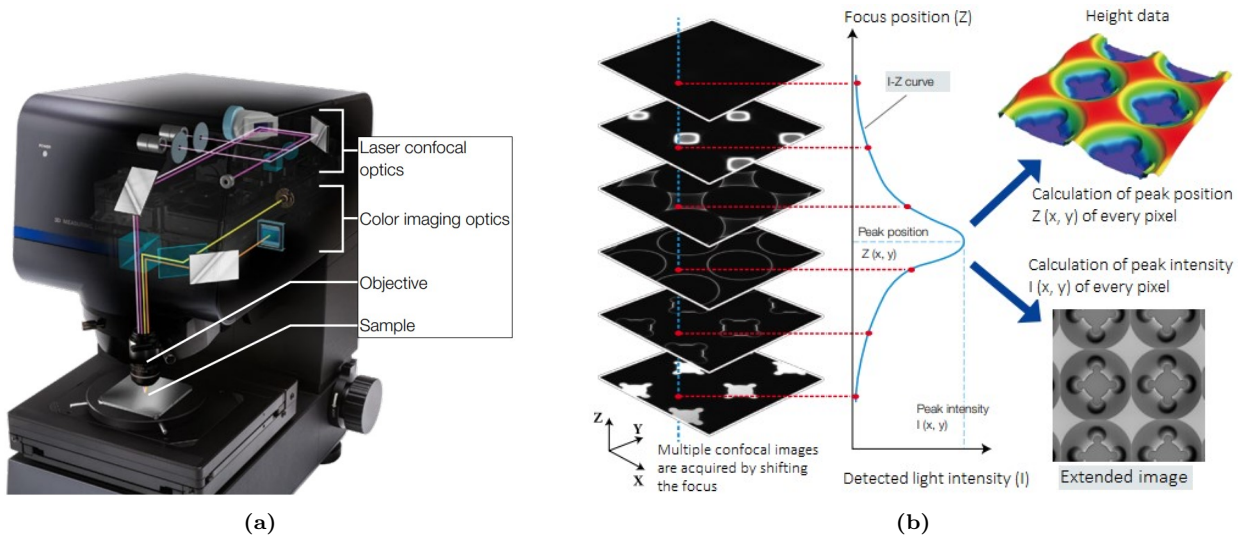

(a) **(b)**

Figure 7: (a) LEXT™ OLS5100 3D Laser Scanning Microscope. (b) Height measurement principle. Reproduced from manufacturer's manual.

The profilometer software provides of a function to display the surface profile and measure the step between any two arbitrary points, width, height, cross-sectional area, and radius, with which the distances, which is used to roughly characterize the structure's features sizes.

(c) Scanning Electron Microscope

The Scanning Electron Microscope (SEM) used to acquire high resolution images is the Thermo Fisher Scientific's model Prisma E SEM.
Given that the samples are made of non-conductive material, before placing them into the SEM chamber a thin layer of silver (20 nm) is sputtered onto the sample, in order to prevent surface charging, i.e. accumulation of electrons on the sample's surface, which would distort the image.

3.1.5 Spectral Scattering Measurements

The measurements to assess the performance of the structures as spectrally dependent light localization devices have been done in another institution: Universitat Politècnica de Catalunya (UPC), Spain, as part of the collaboration with the group of Nonlinear Dynamics, Nonlinear Optics and Lasers (DONLL).
A specific optical set-up was designed in order to perform such measurements, in which a super-continuum laser (Fyla SCT1000) is focused in the structure, and the light scattered upwards is measured with an spectrometer (Kymera 328i) with an IR camera as detector (iDus 1.7µm InGaAs), as depicted in Fig. 8a.

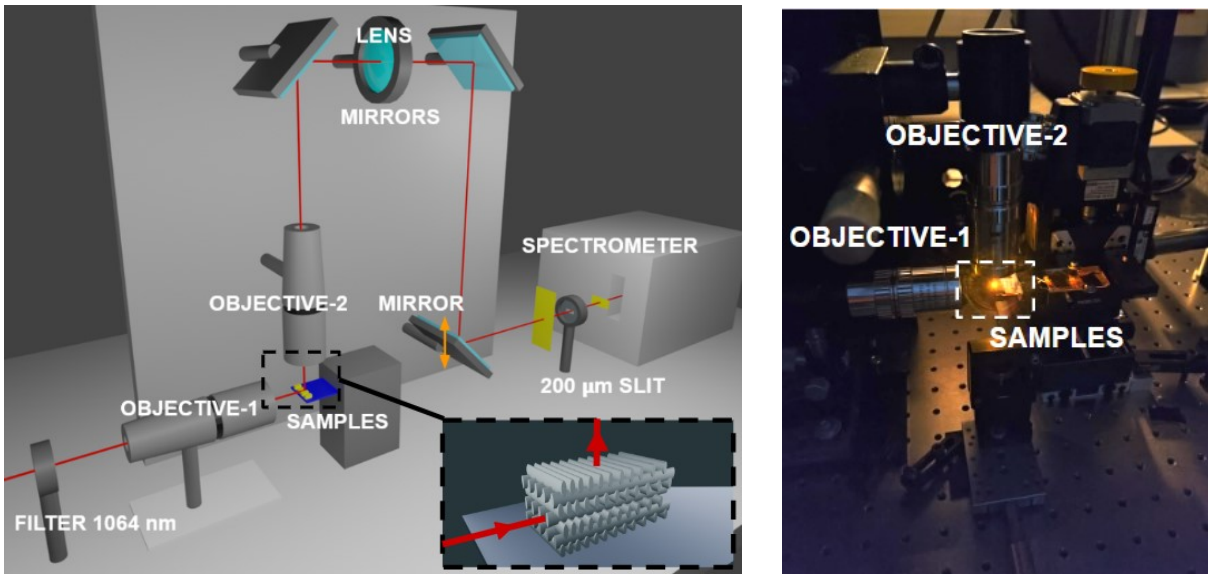

(a) **(b)**

Figure 8: Set-up for IR measurements. (a) Schematic representation. The light scattered upwards is focused into a slit, which only allows a small portion of the formed image (represented as a yellow rectangle) Δz to enter the spectrometer, therefore only viewing the spectrum of that Δz. Reproduced and modified with permission from DONLL group, UPC. (b) Real set-up with the laser focused on the samples.

Both the objective used to focus the laser beam into the sample and the objective used to collect the light scattered upwards, as well as the sample holder, are mounted in stages that can be moved to fine-tune the alignment and proper coupling of the light and the sample and to proper focus its image afterwards. The last mirror is mounted in a motorized stage that allows to displace vertically the image of the sample formed in the spectrometer. And finally, an horizontal slit is placed in front of the spectrometer in order to analyse just the light coming from a specific Δz (different penetration depth), spatially resolving the spectrally dependent light localization.

The main steps of the measurements are the following:

1. The optical set-up is aligned with the laser without the samples.
2. The sample is placed on top of a microscope slide, which is attached afterwards in a holder in front of the first objective and below the second as shown in Fig. 8a.
3. The sample is aligned such that its image is formed in the slit, in such a way that the front facet is right below the slit, which will be the starting point of the measurements.
4. The sample is scanned by moving the moveable mirror with the live acquisition mode of the spectrometer to determine the time acquisition needed and to make sure there are no points in which it will saturate the detectors.
5. The mirror is returned to the origin position defined in step 3.
6. An acquisition of the whole spectrum is taken in that position and the data is saved in a .txt file.

7. The mirror is displaced vertically such that the next Δz of the crystal image goes through the slit, and a new acquisition is taken and saved. This step is repeated until the whole crystal is scanned.

8. The .txt files are used to generate the image of the spectrum through all the crystal.

3.2 Experiments

3.2.1 Familiarization with the Fabrication of 3D Gradient Woodpile Structures

The initial design is presented in Fig. 9, which corresponds to a woodpile of different lattice constants in each direction, with the one along the propagation direction ($\hat{y}$ axis) being gradually varied in the specified range: $\Delta x = 1.0$ µm, $\Delta y = 0.5 - 0.9$ µm and $\Delta z = 0.6$ µm. The dimensions of the structure are 50 x 90 x 50 µm^3, the average power for fabrication is set to $P = 2.5$ mW, and the scanning velocity to $v = 200$ µm/s.

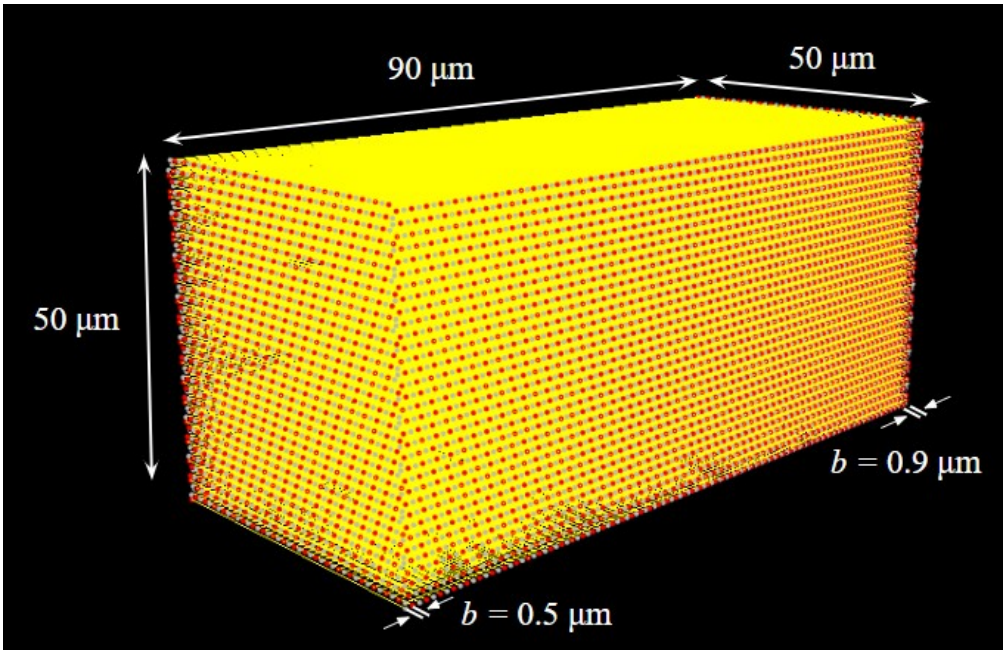

Figure 9: Design of the PhC on the 3DPoli Compiler's 3D preview tab. Red and white points correspond to the positions in which laser shutter is opened/closed.

Actually, the latest design implemented for this project consisted in this woodpile structure supported by spring-like legs, an add-on that was incorporated in order to avoid having the woodpile directly attached to the substrate. This will be implemented in future steps of the study, since it proves to be beneficial for the correct result of the structures, but it's avoided in the initial part of the study given that it adds an extra level of complexity and it has been considered more adequate to start with simpler structures and build up from there.

For the second part of the work, modifications on the design have been done in order to study the impact of the fabrication parameters as well as the structure parameters themselves. A big variety of variables coming into play at each stage of the fabrication process,

which in addition, can result in different outcomes depending on the rest of the parameters, making the research of the optimal values a delicate task. To realize it, two experiments targeting different fabrication parameters have been run in parallel: "Experiment A", dedicated to study the parameters employed during the laser writing stage, and "Experiment B", targeting the design of the structure and the developing process.

3.2.2 Study of Optimal Fabrication Parameters

The exposure dose with which the sample is irradiated plays a major role on the photopolymerization process, having a direct influence on features size and degree of cross-linking, and thus having an impact on rigidity, shrinkage and optical properties of the PhC to name a few. As it depends both on the average laser power and the scanning velocity, it has been considered appropriate to study the variation of both variables conjointly.

For that purpose, a sample consisting of multiple structures arranged in a rectangular grid has been modeled (Fig. 10), for which the power defined to fabricate a single structure is varied along one of the grid's axes with steps of $\Delta P = 0.25$ mW covering the range $P =$ 2.00 – 4.00 mW, and the scanning velocity along the other, in this case $\Delta v = 50$ µm/s and $v = 5$ – 700 µm/s.
In order to simplify the study of the parameters and its analysis, the design of the structures has been reduced/restricted to smaller overall dimensions: 10×10×10 µm^3 (i.e. shorter rods and less amount of layers), and the chirp in the periodicity along the propagation direction has been eliminated and set at $\Delta y = 0.5$ µm (low limit of the initial range), focusing for now the attention on the feature sizes as function of the exposure parameters stated.

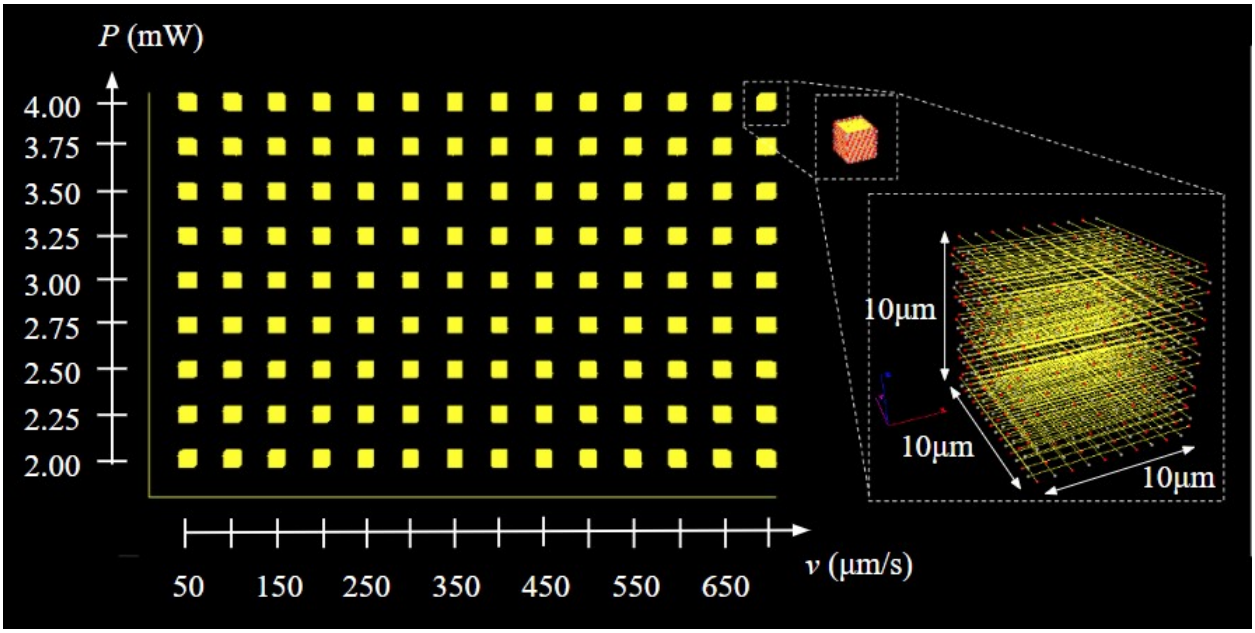

Figure 10: Design of $10 \times 10 \times 10m^3$ woodpiles arranged in a rectangular grid on the 3DPoli Compiler's 3D preview tab together with a zoom view of a single structure. Red and white points correspond to the positions in which laser shutter is opened/closed.

3.2.3 Fabrication of 3D Gradient Photonic Crystal

After studying the size of the features depending on the fabrication parameters, the next step is to fabricate a chirped woodpile suitable for measurements, which requires to increase back the size of the woodpile, which is set to $40 \times 90 \times 40$ µm^3.

In order to demonstrate the effect of the chirp in a 3D periodic structure, a set of three woodpiles with the spring-like supports incorporated is designed, one in which the periodicity along the propagation direction increases adiabatically (positive chirp) from $\Delta y = 0.5$ µm to $\Delta y = 0.9$ µm, one in which the periodicity is kept constant at $\Delta y = 0.7$ µm (no chirp), and one last one in which the periodicity decreases adiabatically (negative chirp) from $\Delta y = 0.9$ µm to $\Delta y = 0.5$ µm.

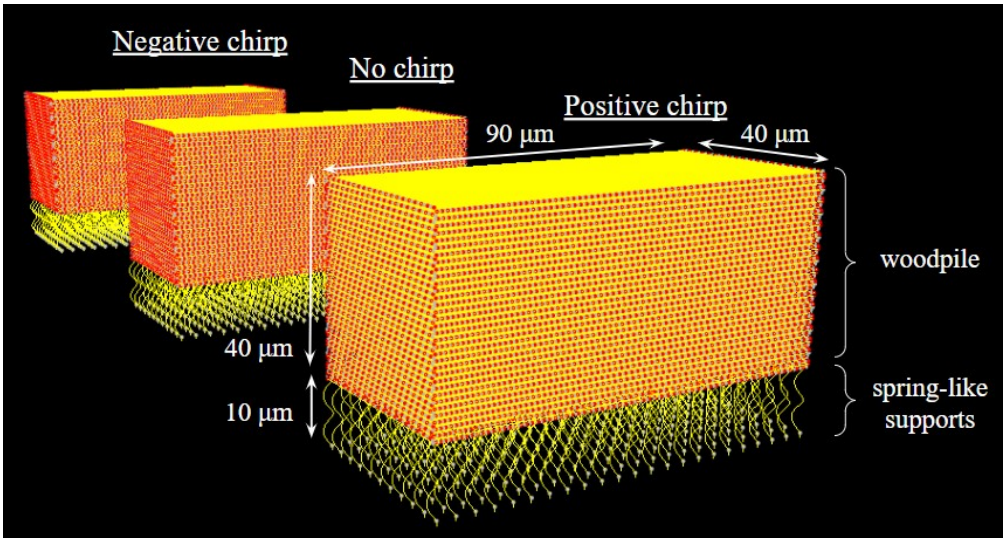

Figure 11: Design of a set of 3 woodpiles consisting of one with positive, one without, and one with negative chirp on the 3DPoli Compiler's 3D preview tab. The woodpiles are of the same dimensions, $40 \times 90 \times 40$ µm^3 and are separated between them a distance 120 µm. Spring-like supports have length L_{sup}. Red and white points correspond to the positions in which laser shutter is opened/closed.

3.3 Numerical Simulations

Numerical simulations have been proven to be powerful tools for modelling, analyzing and optimising devices and systems with considerable cost and time savings, and they have become an important field for the development of innovative optics and photonics.
Most often, for computational electromagnetics, i.e. when numerical simulations are applied for solving electromagnetic problems, the starting point is the set of Maxwell's equations, as they are the analytical expressions that describe how electric and magnetic fields interact, and together with the constitutive relations, how electromagnetic fields propagate in media. Nevertheless, when exact analytical solutions are not available, or when the problem is too complex, numerical techniques offer an alternative to solve the problem.
For this work, different numerical methods have been used to model and simulate different features of the electromagnetic fields' behaviour in the presented structure by numerically

solving Maxwell's equations in dielectric periodic media.

To begin with, the Plane Wave Expansion Method (PWEM) has been implemented in Matlab to study the dispersion relation of the photonic crystal. Following up, the Rigorous Coupled-Wave Analysis approach (RCWA) has been performed in Python to analyse the reflection and transmission of the structure. Finally, Ansys Lumerical Simulation Software has been used to simulate the propagation of the electric field inside the structures for different wavelengths via Finite Diference Time Domain (FDTD) method.
The first couple ones, i.e. PWEM and RCWA, have been written starting from codes used during the Computational Photonics lectures, which have been modified and adapted to the current problem. On the other side, FDTD main simulation has been provided from the partners of the project, and minor modifications have been done in order to obtain the results for the corresponding structures.

3.3.1 Plane Wave Expansion Method

The PWEM is a method based on the expansion of electromagnetic fields and permittivity functions into time and space Fourier series (frequency domain and Fourier space), which simplifies the analysis of periodic complex structures. Following that, the fields are represented as a sum of plane waves at different angles and different wavelengths named "spatial harmonics",

$$\boldsymbol{E}(\boldsymbol{r}) = \sum_{p=-\infty}^{\infty}\sum_{q=-\infty}^{\infty}\sum_{r=-\infty}^{\infty} \boldsymbol{S}(p,q,r)e^{-j[k_x(p,q,r)x+k_y(p,q,r)y+k_z(p,q,r)z]} \tag{12}$$

$$\tilde{\boldsymbol{H}}(\boldsymbol{r}) = \sum_{p=-\infty}^{\infty}\sum_{q=-\infty}^{\infty}\sum_{r=-\infty}^{\infty} \boldsymbol{U}(p,q,r)e^{-j[k_x(p,q,r)x+k_y(p,q,r)y+k_z(p,q,r)z]} \tag{13}$$

where $\boldsymbol{E}(\boldsymbol{r})$ is the electric field, $\tilde{\boldsymbol{H}}(\boldsymbol{r})$ the normalized magnetic field[1], and $\boldsymbol{S}(p,q,r)$ and $\boldsymbol{U}(p,q,r)$ the corresponding amplitudes of the plane wave decomposition, being p,q,r the indexes characterizing the wavevector $\boldsymbol{k}(p,q,r) = (\boldsymbol{k_x},\boldsymbol{k_y},\boldsymbol{k_z}) = \boldsymbol{\beta} - p\boldsymbol{T}_1 - q\boldsymbol{T}_2 - r\boldsymbol{T}_3$, for which it has been taken into account that the fields inside the periodic media must fulfill Bloch's theorem, and that Bloch waves are described by a plane wave of wavevector $\boldsymbol{\beta}$ modulated by a periodic function:

$$\boldsymbol{E}(\boldsymbol{r}) = e^{-j\boldsymbol{\beta}\cdot\boldsymbol{r}}\sum_{p=-\infty}^{\infty}\sum_{q=-\infty}^{\infty}\sum_{r=-\infty}^{\infty} \boldsymbol{S}(p,q,r)e^{j(p\boldsymbol{T}_1+q\boldsymbol{T}_2+r\boldsymbol{T}_3)\cdot\boldsymbol{r}} \tag{14}$$

and the periodic dielectric media is represented as the sum of sinusoidal gratings at different angles and periods by expanding the permittivity function into spatial Fourier series

$$\varepsilon_{\mathrm{r}}(\boldsymbol{r}) = \sum_{p=-\infty}^{\infty}\sum_{q=-\infty}^{\infty}\sum_{r=-\infty}^{\infty} a(p,q,r)e^{j(p\boldsymbol{T}_1+q\boldsymbol{T}_2+r\boldsymbol{T}_3)\cdot\boldsymbol{r}} \tag{15}$$

[1]Normalized as $\tilde{\boldsymbol{H}} = -j\sqrt{\frac{\mu_0}{\epsilon_0}}\boldsymbol{H}$

These expressions are introduced into Maxwell's equations and after performing some algebra, they can be rearranged and written in block matrix form, leading to an eigen-value problem in which the solution (the eigen-value) is the frequency, and the eigen-vectors are the modes.

$$\underline{\text{Real space}} \qquad (16) \qquad \underline{\text{Fourier space}} \qquad (17)$$

$$\frac{\partial \tilde{H}_z}{\partial y} - \frac{\partial \tilde{H}_y}{\partial z} = k_0 \varepsilon_r E_x \qquad \mathbf{K}_y \mathbf{u}_z - \mathbf{K}_z \mathbf{u}_y = j k_0 [\![\varepsilon_r]\!] \mathbf{s}_x$$

$$\frac{\partial \tilde{H}_x}{\partial z} - \frac{\partial \tilde{H}_z}{\partial x} = k_0 \varepsilon_r E_y \qquad \mathbf{K}_z \mathbf{u}_x - \mathbf{K}_x \mathbf{u}_z = j k_0 [\![\varepsilon_r]\!] \mathbf{s}_y$$

$$\frac{\partial \tilde{H}_y}{\partial x} - \frac{\partial \tilde{H}_x}{\partial y} = k_0 \varepsilon_r E_z \qquad \mathbf{K}_x \mathbf{u}_y - \mathbf{K}_y \mathbf{u}_x = j k_0 [\![\varepsilon_r]\!] \mathbf{s}_z$$

$$\frac{\partial E_z}{\partial y} - \frac{\partial E_y}{\partial z} = k_0 \varepsilon_r \tilde{H}_x \qquad \mathbf{K}_y \mathbf{s}_z - \mathbf{K}_z \mathbf{s}_y = j k_0 [\![\mu_r]\!] \mathbf{u}_x$$

$$\frac{\partial E_x}{\partial z} - \frac{\partial E_z}{\partial x} = k_0 \varepsilon_r \tilde{H}_y \qquad \mathbf{K}_z \mathbf{s}_x - \mathbf{K}_x \mathbf{s}_z = j k_0 [\![\mu_r]\!] \mathbf{u}_y$$

$$\frac{\partial E_y}{\partial x} - \frac{\partial E_x}{\partial y} = k_0 \varepsilon_r \tilde{H}_z \qquad \mathbf{K}_x \mathbf{s}_y - \mathbf{K}_y \mathbf{s}_x = j k_0 [\![\mu_r]\!] \mathbf{u}_z$$

Compact Block Matrix Notation

$$[\boldsymbol{K}\times] \left[[\![\mu_r]\!]\right]^{-1} [\boldsymbol{K}\times] \, \boldsymbol{s} = -k_0^2 \left[[\![\varepsilon_r]\!]\right] \boldsymbol{s} \qquad (18)$$

One important thing is that this method works for periodic structures. As mentioned previously, the structure of interest for this study is not completely periodic, a chirp in the lattice constant in the direction of propagation is introduced in order to achieve the desired effect, reason why it's not possible to simulate such device exactly. What is done instead, is to define the device with a constant lattice, for instance the smallest lattice constant present in the structure, and perform a sweep covering all the range present in the structure. The result will approximate how the dispersion relation, and therefore the modes and band gaps, evolves along its propagation inside the structure, considering that the variation of the lattice constant changes so slowly that the structure maintains its photonic crystal properties, but when analyzing them locally, they present minimal differences.

This method has been used to visualize the photonic band diagram of the structure. By sweeping the lattice constant b on the range present in the chirped structure, the local dispersion relation at each position along the propagation can be calculated, knowing that there is a direct link between the local lattice constant b and the position z. Considering this, it is possible to assess how the band gap evolves, as well as the group velocity of a specific wavelength at a specific position inside the crystal, which allows to simulate how the velocity of propagation of a given wavelength will evolve as it propagates further inside the crystal.

3.3.2 Rigorous Coupled Wave Analysis

RCWA is somewhat similar to PWEM, but it has a crucial difference compare to the previous one. This method also makes use of Fourier expansions, but in this case just in the transverse coordinates, the parameter z remaining analytical keeping the longitudinal direction (thus the propagation) analytical, reason why it's considered a semi-analytical method. As in the PWEM, Maxwell's equations are written in block matrix form,

$$\underline{\text{Real space}} \qquad\qquad \underline{\text{Fourier space}}$$

$$\begin{aligned}
\frac{\partial \tilde{H}_z}{\partial y} - \frac{\partial \tilde{H}_y}{\partial z} &= k_0 \varepsilon_r E_x & -j\mathbf{K}_y \mathbf{u}_z - \frac{d}{d\tilde{z}}\mathbf{u}_y &= k_0 [\![\varepsilon_r]\!] \mathbf{s}_x \\
\frac{\partial \tilde{H}_x}{\partial z} - \frac{\partial \tilde{H}_z}{\partial x} &= k_0 \varepsilon_r E_y & \frac{d}{d\tilde{z}}\mathbf{u}_x + j\mathbf{K}_x \mathbf{u}_z &= k_0 [\![\varepsilon_r]\!] \mathbf{s}_y \\
\frac{\partial \tilde{H}_y}{\partial x} - \frac{\partial \tilde{H}_x}{\partial y} &= k_0 \varepsilon_r E_z & \mathbf{K}_x \mathbf{u}_y - \mathbf{K}_y \mathbf{u}_x &= j k_0 [\![\varepsilon_r]\!] \mathbf{s}_z \\
& \qquad (19) & & \qquad (20) \\
\frac{\partial E_z}{\partial y} - \frac{\partial E_y}{\partial z} &= k_0 \varepsilon_r \tilde{H}_x & -j\mathbf{K}_y \mathbf{s}_z - \frac{d}{d\tilde{z}}\mathbf{s}_y &= k_0 [\![\varepsilon_r]\!] \mathbf{u}_x \\
\frac{\partial E_x}{\partial z} - \frac{\partial E_z}{\partial x} &= k_0 \varepsilon_r \tilde{H}_y & \frac{d}{d\tilde{z}}\mathbf{s}_x + j\mathbf{K}_x \mathbf{s}_z &= k_0 [\![\varepsilon_r]\!] \mathbf{u}_y \\
\frac{\partial E_y}{\partial x} - \frac{\partial E_x}{\partial y} &= k_0 \varepsilon_r \tilde{H}_z & \mathbf{K}_x \mathbf{s}_y - \mathbf{K}_y \mathbf{s}_x &= j k_0 [\![\varepsilon_r]\!] \mathbf{u}_z
\end{aligned}$$

but this time, the equation obtained after performing some algebra it corresponds to a (Block matrix) wave equation:

$$\frac{d^2}{d\tilde{z}^2} \begin{bmatrix} \boldsymbol{s}_x \\ \boldsymbol{s}_y \end{bmatrix} - \boldsymbol{\Omega}^2 \begin{bmatrix} \boldsymbol{s}_x \\ \boldsymbol{s}_y \end{bmatrix} = \mathbf{0} \tag{21}$$

being $\boldsymbol{\Omega}$ a matrix resulting from the product of two block matrices that contain $\tilde{\boldsymbol{K}}_x$, $\tilde{\boldsymbol{K}}_y$ matrices and $[\![\varepsilon_\mathrm{r}]\!]$, $[\![\mu_\mathrm{r}]\!]$ matrices and their inverse. which has for solution a forward propagating and a backward propagating waves:

$$\begin{bmatrix} \boldsymbol{s}_x(\tilde{z}) \\ \boldsymbol{s}_y(\tilde{z}) \end{bmatrix} = e^{-\boldsymbol{\Omega}\tilde{z}} \boldsymbol{s}^+(0) + e^{\boldsymbol{\Omega}\tilde{z}} \boldsymbol{s}^-(0) \tag{22}$$

in which the same nomenclature as in the formulation of PWEM is used, where $\boldsymbol{s}_x$, $\boldsymbol{s}_y$ designates the expansion coefficients of the electric field.

Matrix $\boldsymbol{\Omega}$ is not a diagonal matrix but it is an square one, so it's possible to diagonalize and the solutions of the wave equation can be written in terms of its eigenvectors and eigenvalues by applying the following relation from matrix algebra:

$$f(\mathbf{A}) = \mathbf{W} \cdot f(\boldsymbol{\lambda}) \cdot \mathbf{W}^{-1} \qquad \rightarrow \qquad e^{-\boldsymbol{\Omega}\tilde{z}} = \mathbf{W} e^{-\lambda \tilde{z}} \mathbf{W}^{-1}, \quad e^{\boldsymbol{\Omega}\tilde{z}} = \mathbf{W} e^{\boldsymbol{\lambda}\tilde{z}} \mathbf{W}^{-1} \tag{23}$$

being $\mathbf{W}$ the eigen-vector matrix and $\boldsymbol{\lambda}^2$ the eigen-value matrix of $\boldsymbol{\Omega}^2$.

The terms $\boldsymbol{s}^+(0)$ $\boldsymbol{s}^-(0)$ are initial values that are not yet calculated, and they are combined with $\mathbf{W}^{-1}$ to produce column vectors of proportionality constants c^+ and c^-, such that the solutions are of the form:

$$\begin{bmatrix} \boldsymbol{s}_x(\tilde{z}) \\ \boldsymbol{s}_y(\tilde{z}) \end{bmatrix} = \mathbf{W}e^{-\boldsymbol{\lambda}\tilde{z}}\boldsymbol{c}^+ + \mathbf{W}e^{\boldsymbol{\lambda}\tilde{z}}\boldsymbol{c}^- \tag{24}$$

An analogous solution is found for the magnetic field, and they are combined into a single vector and matrix form.

$$\boldsymbol{\Psi}(\tilde{z}) = \begin{bmatrix} \boldsymbol{s}_x(\tilde{z}) \\ \boldsymbol{s}_y(\tilde{z}) \\ \boldsymbol{u}_x(\tilde{z}) \\ \boldsymbol{u}_y(\tilde{z}) \end{bmatrix} = \begin{bmatrix} \mathbf{W} & \mathbf{W} \\ -\mathbf{V} & \mathbf{V} \end{bmatrix} \begin{bmatrix} e^{-\boldsymbol{\lambda}\tilde{z}} & \mathbf{0} \\ \mathbf{0} & e^{-\boldsymbol{\lambda}\tilde{z}} \end{bmatrix} \begin{bmatrix} \boldsymbol{c}^+ \\ \boldsymbol{c}^- \end{bmatrix}, \qquad \text{where} \quad \mathbf{V} = \mathbf{Q}\mathbf{W}\boldsymbol{\lambda}^{-1} \tag{25}$$

$\mathbf{V}$ being the analogue of $\mathbf{W}$ for the magnetic waves.

To propagate the wave through the whole structure, the Transfer Matrix Method is used. The solutions mentioned above describe the field inside one of the layers, and by using a scattering matrix, a relation between the boundary conditions is defined such that the reflection and transmission of the device can be obtained by working through the device one layer at a time and calculating an overall scattering matrix.

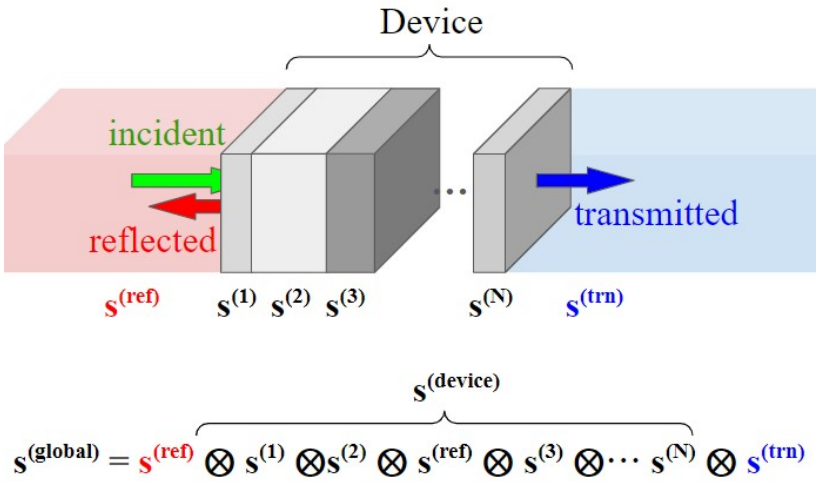

Figure 12: Scattering matrix principle

Using this method, the reflection and transmission of the structure have been simulated for different wavelengths at normal incidence (same incidence considered when studying the band gap and group velocity), and later on for different angles and frequencies.

3.3.3 Finite Difference Time Domain

As oppositely to the previous ones, Finite Difference Time Domain method is, as its name indicates, not in frequency but in time domain, and it keeps also the spatial coordinates in the real domain.

In order to numerically manipulate Maxwell's equations both time and space are discretized and the derivatives are calculated taking the central difference approximation, as exemplified in Eq. (26) for the Ampere law in 1D

$$\frac{\partial E_x}{\partial t} = -\frac{1}{\varepsilon_0}\frac{\partial H_y}{\partial z} \qquad \rightarrow \qquad \frac{E_x^{n+1/2}(k) - E_x^{n-1/2}(k)}{\Delta t} = -\frac{1}{\varepsilon_0}\frac{H_y^n(k+\frac{1}{2}) - H_y^n(k-\frac{1}{2})}{\Delta z} \tag{26}$$

This formulation is done by using the Yee grid, a staggered grid in which the **E** and **H** field components are interleaved both in space and time

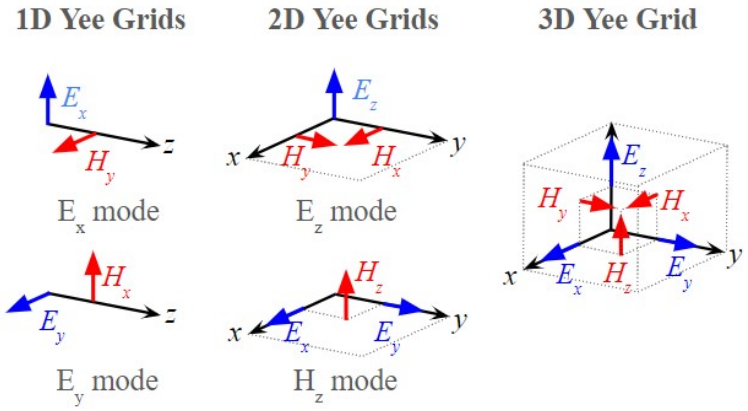

Figure 13: Yee grid cells.

which provides of an elegant arrangement to approximate Maxwell's curl equations and that is divergence-free by itself. Nevertheless, field components are allocated in different physical positions, which may result in field components residing in different materials even if they are in the same unit cell.

This method hasn't been implemented by raw coding, but with a software provided by Ansys Lumerical, which simplifies the task of modeling. The rods are described by cylinders, already defined in Lumerical, and arranged following the structure configuration.
Given that the structure is completely periodic in the coordinates tangential to the propagation, it's possible to restrict the simulation to a unit cell and make use of periodic boundary conditions. On the other hand, for the coordinate normal to propagation, the whole structure is implemented, and a Perfectly Matched Layer (PML) is applied in order to simulate open boundary conditions, i.e., to represent the wave propagating to infinite after leaving the crystal.
Regarding the light source, a pulse of a certain bandwidth propagates towards positive $\hat{y}$ with a plane wavefront, and the response over the corresponding range of frequencies is recovered afterwards by doing a Fourier transform of the time dependent fields.

4 Results and Discussion

4.1 Fabrication

4.1.1 Characterization of 3D Gradient Woodpile Structures

The structure was first analysed with the optical microscope, as well as with the scanning profilometer, and finally with the SEM, which provides of a clearer, more detailed and more complete view of the structures.

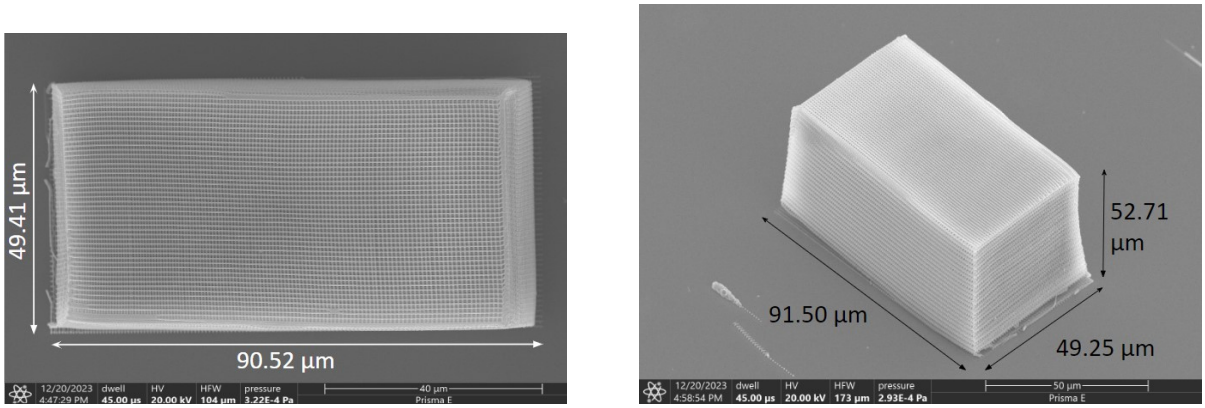

(a) **(b)**

Figure 14: SEM images of the printed structure corresponding to initial design. (a) top view (b) 45° rotation, 45° tilt view. Comment: lines in the substrate next to the structure correspond to marks done while searching the interface during fabrication stage.

As it can be observed in Fig. 14, there are deformations and defects present on the structure, being the most relevant ones: a not uniform shrinkage from bottom to top, a different degree of shrinkage on the top layers depending on the rods periodicity (the region in which the periodicity is smaller, i.e. where the density of rods is higher, appears to remain less affected), and the detachment of the structure from the substrate.
All of them are attributed to the shrinkage of the polymerized material and the tension and stress forces present in the structure, bringing to light the need of supports that fix the structures to the substrate while allowing the bottom layers to shrink as freely as the top layers. By increasing magnification, it is possible to observe with high resolution the rod dimensions as well as its periodicity.

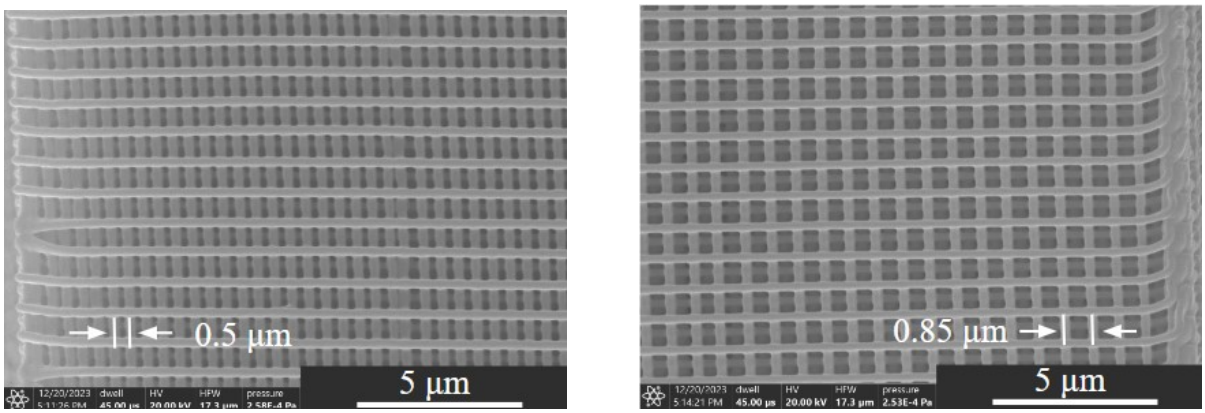

(a) (b)

Figure 15: SEM images with higher magnification of the printed structure corresponding to initial design. (a) left side region (b) right side region.

From these images (Fig. 15) it can be concluded that in the overall, the structure fabricated reproduces quite successfully the intended design, presenting uniform rod widths and a consistent periodicity. Nevertheless, some defects can be observed, like the attachment between neighbouring rods or not well-defined distributions along the edges.
These defects have been left to study in further detail in the second experiment, in which the scanning speed and laser power are tested.

4.1.2 Study of Optimal Fabrication Parameters

The images obtained with the optical microscope (Fig. 16) provide of enough visual information to make a first triage of the samples. From them, it can be clearly observed the threshold character of the fabrication process: while low intensity may not result in a sufficient degree of cross-linking for the structure to survive the development stage, an excessive amount of it can result in polymer damage. The samples in the diagonal (bottom left to top right of Fig. 16) appear to be fabricated within the polymerization window, whereas the structures out of that diagonal, i.e. the lower-right region/upper-left region, appear to be beneath/above the fabrication thresholds, in other words, they appear to be under/over exposed.

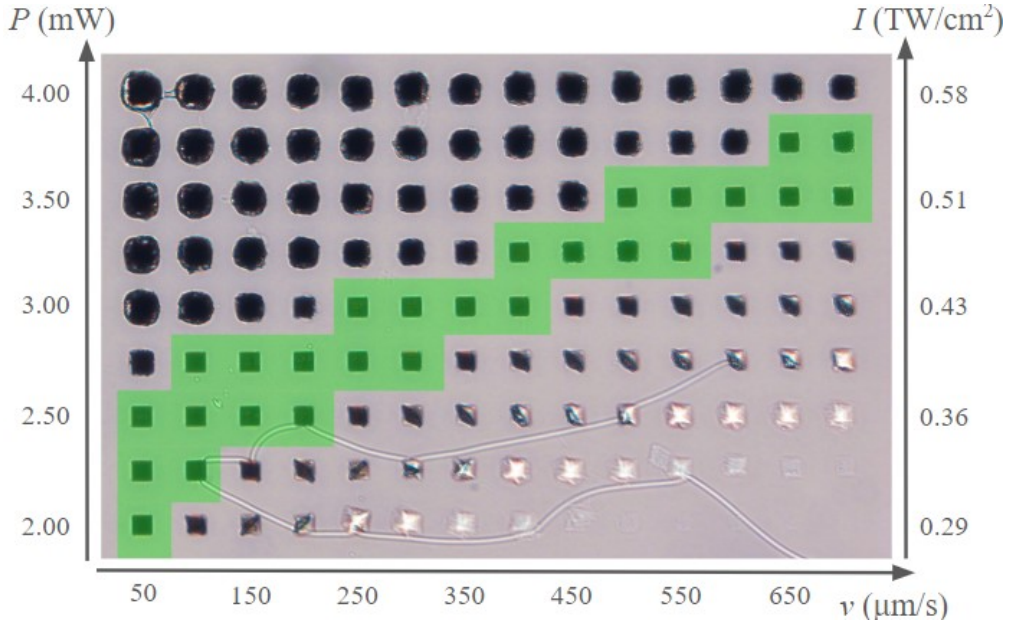

Figure 16: Optical microscope images of structures fabricated using different powers P and velocities v. Comment: the filament observed on the bottom is the detached grid's frame.

Following the same course of action as for the first structure, the sample is sputter coated with silver and observed in the SEM. Given the considerable amount of structures present in the sample, the most representative ones have been selected to present/illustrate the trends exhibited, since big part of them were simply burned out or under-exposed (as it can already be observed from the previous characterization methods), and it has been considered unnecessary to overfill the report with images that do not provide of relevant or new information.

A sequence of structures fabricated using the same scanning velocity $v = 150$ µm/s but different average laser power is presented to show the impact of the exposure intensity on the structure's shape, corresponding to Fig. 17:

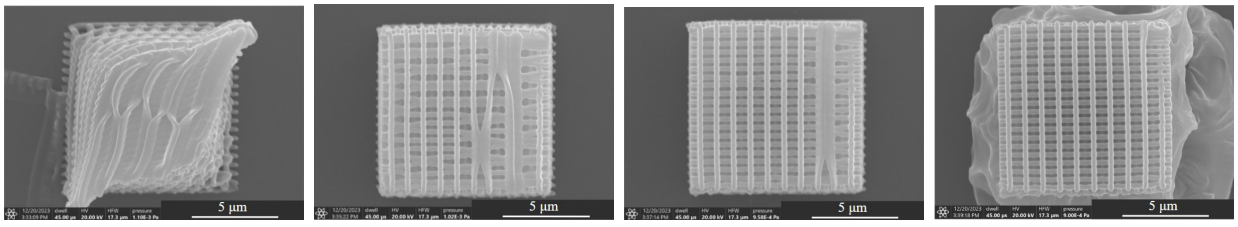

(a) **(b)** **(c)** **(d)**

Figure 17: Resulting structures fabricated using different powers. SEM images of structures fabricated using a constant velocity $v = 150$ µm/s and powers: (a) $P = 2.25$ mW (b) $P = 2.50$ mW. (c) $P = 2.75$ mW. (d) $P = 3.00$ mW.

These results give an idea of up to which point the fabrication parameters to obtain the desired structures are restricted to a small range of values: while using low intensities may not result in a sufficient degree of cross-linking for the structure to have enough mechanical strength to resist the development stage without deforming, an excessive amount of it can

induce polymerization outside the focus region and/or polymer damage, restricting the range of powers and velocities to an even tinier range that the one defined by the polymerization window. This range will be referred to as dynamic fabrication range, standing for that set of values that result in fabricated structures that reproduce the design of the model.

An important observation is that the rods of the structures fabricated using high velocities appear irregular, ondulated, and they show a higher amount of rods attached to their neighbours, as it can be observed in Fig. 18b, whereas on the other side, the rods of the structures fabricated at slower velocities and smaller powers present straight line shapes, resulting in a smaller amount of defects, Fig. 18a. This has been attributed to the fact that the trajectory/movement of the stages is more precise the slower they move, and in light of this, the dynamic fabrication range has been narrowed to those combinations of P and v that provide of the optimal degree of cross-linkage with slow scanning velocities.

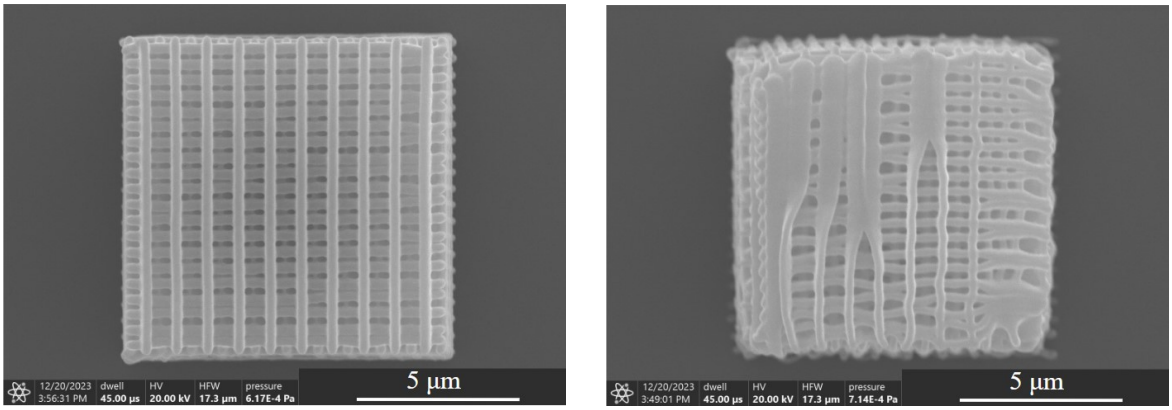

(a) **(b)**

Figure 18: Comparison of structures fabricated at slow velocity and low power vs fast velocity and high power. SEM images of structures fabricated with (a) $P = 2.25$ mW and $v = 50$ µm/s. (b) $P = 3.50$ mW and $v = 500$ µm/s.

From here, a more profound study of the parameters has been restricted to a smaller range of P and v over which the samples show the less deformations, which has been narrowed to printing parameters in range $P = 2 - 3$ mW and $v = 50 - 200$ µm/s.

The elements that have been measured in order to compare the feature parameters depending on power and speed are: the widths of the rods ($d_{x,y}$), the distance at which they are separated , i.e. the periodicity (Δx, Δy), and the lateral dimensions of the whole structure ($L_{x,y}$), which are all relevant parameters that will determine the optical performances of the PhC. To assess the influence of power on feature size, structures fabricated using an scanning speed $v = 50$ µm/s are the ones used for the measurements, whereas samples fabricated with an average laser power $P = 2.50$ mW have been taken to assess the impact of fabricating at different speeds. The reason why these specific structures are the ones for which characterization is done is because they were the cases in which more exemplars inside the dynamic power range and dynamic exposure range was found. The images used for this analysis together with the corresponding lines of the measurements are presented in Fig. 19

and Fig. 20. The data extracted from them is presented in Table 1, 2.

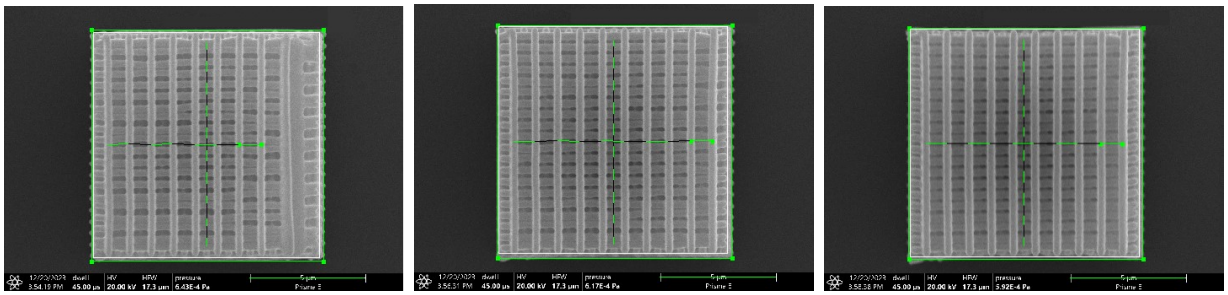

(a) **(b)** **(c)**

Figure 19: SEM images of structures fabricated using constant velocity $v = 50$ µm/s and varying power P. (a) $P = 2.00$ mW. (b) $P = 2.25$ mW. (c) $P = 2.50$ mW.

It's possible to observe directly from the images that the structures suffer from a greater shrinkage (even though still minor) on the upper layers than on the lower ones, which is the reason why two sets of measures have been taken to assess their dimensions: one corresponding to the bottom layer (corresponding to subindex 1), and the other to the upper (subindex 2). To quantitatively analyse the shrinkage suffered, the variation respect to the model has been computed and it's presented in the same table "Dev. $Lx_{1,2}, y_{1,2}$".
On the other side, the averaged value of the measures extracted from each individual rod is the one taken into consideration when comparing the results obtained using different printing parameters, (a single measure of each individual rod has been measured on the top layer where the arrangement of rods is visible), and the standard deviation of the set is used to give an estimation of their variability/uncertainty.

Table 1: Physical dimensions of the structures depending on average laser power, measured from Fig. 19. (a) Woodpile dimensions. (b) Rod dimensions and periodicity.

(a)

Fig.	Power (mW)	Lx_1 (µm)	Ly_1 (µm)	Lx_2 (µm)	Ly_2 (µm)	Dev. Lx_1 (%)	Dev. Ly_1 (%)	Dev. Lx_2 (%)	Dev. Ly_2 (%)
19a	2.00	10.06	10.00	9.80	9.64	+ 0.63	- 0.02	- 1.97	- 2.62
19b	2.25	10.13	10.03	9.87	9.77	+ 1.28	+ 0.30	- 1.32	- 2.30
19c	2.50	10.14	9.98	9.92	9.85	+ 1.44	- 0.19	- 0.84	- 1.49

(b)

Fig.	Power (mW)	$d_{x,av}$ (µm)	$d_{y,av}$ (µm)	Δx_{av} (µm)	Δy_{av} (µm)	Dev. Δx_{av} (%)	Dev. Δy_{av} (%)
19a	2.00	0.308 ± 0.024	0.307 ± 0.027	0.948 ± 0.015	0.464 ± 0.076	5.16	7.14
19b	2.25	0.334 ± 0.019	0.331 ± 0.022	0.949 ± 0.015	0.474 ± 0.054	5.07	5.13
19c	2.50	0.360 ± 0.016	0.336 ± 0.026	0.944 ± 0.021	0.469 ± 0.045	5.56	6.21

One important observation from the results presented in Table 1 is that the woodpile dimensions evaluated on the bottom layers, present again larger values than the ones of the model (described by positive values in the deviation). This has been attributed to two factors: first, a small and almost negligible shrinkage, which can be explained by the presence of adhesion forces between the substrate and the polymer counteracting the shrinkage stress,

and second, the non-zero dimensions of the rods (which is not accounted for in the model code), which if added to a non-shrinked structure, can result in larger dimensions.
Antoher important observation regarding the shrinkage of the top layers is that the bigger the laser average power, the less the shrinkage appears to be.

On the other hand, an increasing average laser power appears to result in an increment in the rod's widths, whereas no apparent significant variation can be observed regarding the periodicity.

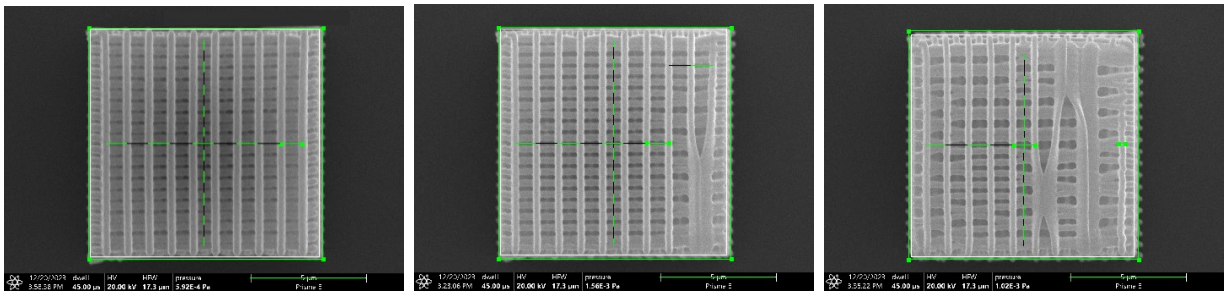

(a) **(b)** **(c)**

Figure 20: SEM images of structures fabricated using constant power $P = 2.50$ mW and varying velocity v. (a) $v = 50$ µm/s. (b) $v = 100$ µm/s. (c) $v = 150$ µm/s.

As it can be observed in Fig. 20, this other set of structures show more structural defects than the previous, supporting again the conclusion that higher scanning speeds result in less precision of the rod's fabrication.

Table 2: Physical dimensions of the structures depending on laser scanning speed, measured from Fig. 20. (a) Woodpile dimensions. (b) Rod dimensions and periodicity.

(a)

Fig.	Velocity (µm/s)	Lx_1 (µm)	Ly_1 (µm)	Lx_2 (µm)	Ly_2 (µm)	Dev. Lx_1 (%)	Dev. Lx_1 (%)	Dev. Lx_2 (%)	Dev. Ly_2 (%)
20a	50	10.14	9.98	9.92	9.85	+ 1.44	- 0.19	- 0.84	- 1.49
20b	100	10.05	9.97	9.75	9.74	+ 0.46	- 0.35	- 2.46	- 2.62
20c	150	9.95	9.84	9.62	9.54	- 0.51	-1.65	- 3.76	- 4.57

(b)

Fig.	Velocity (µm/s)	$d_{x,av}$ (µm)	$d_{y,av}$ (µm)	Δx_{av} (µm)	Δy_{av} (µm)	Dev. Δx_{av} (%)	Dev. Δy_{av} (%)
20a	50	0.360 ± 0.016	0.336 ± 0.023	0.944 ± 0.021	0.469 ± 0.045	5.56	6.21
20b	100	0.302 ± 0.014	0.308 ± 0.015	0.948 ± 0.017	0.465 ± 0.066	5.16	6.98
20c	150	0.279 ± 0.008	0.283 ± 0.030	0.935 ± 0.045	0.460 ± 0.154	6.50	8.00

Oppositely to the previous case, an increase on this variable (scanning velocity) appears to result in a higher degree of shrinkage and a smaller rod's width, while similarly to the analysis of variation on power, no clear conclusions can be derived regarding periodicities.

4.1.2.1 Re-calibration of the fabrication parameters

Once this study was completed, an additional software was installed in the working station used for the fabrication, Femtika's Laser Nanofactory, and some parameters were modified, for which a new inspection of the fabrication parameters was requiered, Fig. 21a.
Together with it, the incorporation of spring-like supports was also implemented in a 2×2 array sweeping along the same values of P and v, Fig. 21b, and before developing them, a single chirped woodpile of dimensions 40×90×40 µm^3 was fabricated on the same droplet with $P = 3.25$ mW and $v = 90$ µm/s, in order to check that the result for a specific (P, v) for smaller woodpiles was scalable to bigger woodpiles with the chirp[2].

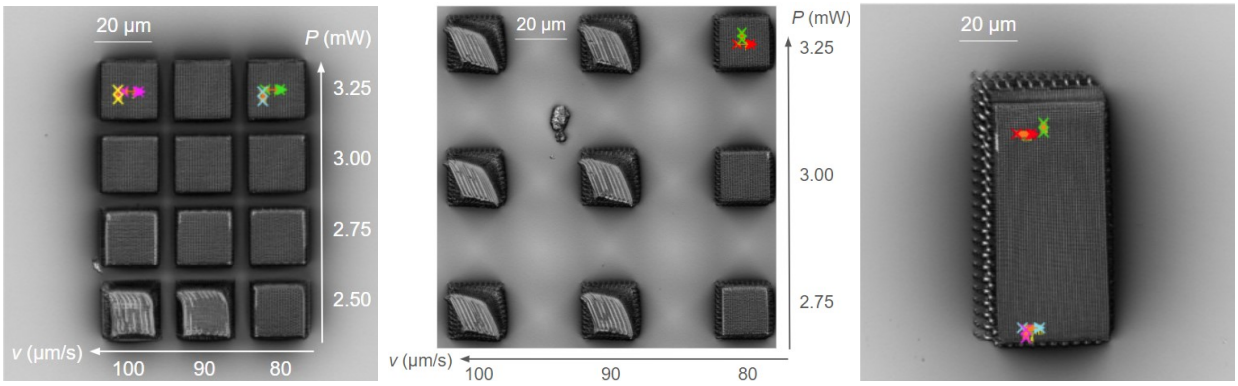

(a) **(b)** **(c)**

Figure 21: Optical scanning profilometer images using objective's magnification 100x. (a-b) structures of dimensions 20×20×20 µm^3 fabricated using different powers, P and velocties, v. (a) Woodpiles without supports. Separation between woodpiles: 25 µm. (b) Woodpiles with spring-like supports. Separation between woodpiles: 50 µm. (c) Chirped woodpile structure of 40×90×40 µm^3 with surface profile lines used for characterization.

As it can be observed in Fig. 22, the structures fabricated with spirals supports turned out to be less robust than their analogous woodpiles fabricated in direct contact with the substrate, but the chirped woodpile survived better the development than the small woodpile fabricated with the same power and scanning velocity.

After lots of fabrications, it was observed that even when using the same fabrication parameters, slightly different results were obtained. This had been mostly attibuted to different degrees of condensation of the pre-polymer. Even though the procedure followed for their preparation was the same, different batches of samples were prepared and used after different amounts of days depending on the availability of the Laser Nanofactory, which might have modestly influenced the state of the material.
In addition, another setback encountered was that the pre-polymer was showing signals of aging and a new bottle of SZ2080™ was sent, which was less viscous and was resulting in donut-shape droplets, for which the procedure for preparing of the sample had to be modified, and was solved by drop-casting a second droplet on top of initial. It was later realized that by pre-heating the substrate before drop-casting the SZ2080™ it was possible to achieve

[2]The choice of these values was taken considering that no elements appeared over-exposed in the arrays, which is something visible before the developing, and to minimize the risk of uncontrolled polymerization when scaling the size of the woodpiles, the intermediate velocity that was explored in the arrays was chosen.

a dome-shape droplet as with the old resin, and the next sets of samples were done this way.

Nevertheless, the optimal parameters for the fabrication do not vary enormously, for which after this "re-calibration", the fabrications were always kept inside the same range of $P = 2.5$ – 4 mW and the velocities below 90 µm/s and above 50 µm/s.

4.1.3 3D Gradient Woodpile Photonic Crystal

Once the range of optimal parameters was defined, the fabrication of the spirals was studied in further detail.

The velocity at which the laser moves for the fabrication of the spring-like supports was set slower than for the straight rods of the woodpile, at a speed $v_{sup} = 10$ µm/s and the power was lowered to $P_{sup} = 2.5$ mW. As it can be seen in Fig. 21c the supports appear to let the woodpiles move too freely and not keep them stable on top of them, for which the length of the supports was tested out, aiming to study if shorter supports are more adequate for their purpose without changing the exposure parameters.
Actually, the length of the supports was kept the same in order to not change the shape of the spirals, but they were buried deeper inside the glass, i.e. leaving shorter spring-like supports fabricated in the resin.
Considering that for the first samples in which the spring-like supports were included the length was $L_{sup} = 10$ µm, three different lengths were studied: $L_{sup} = 5, 10, 15$ µm, the result of which is presented in Fig. 22a.

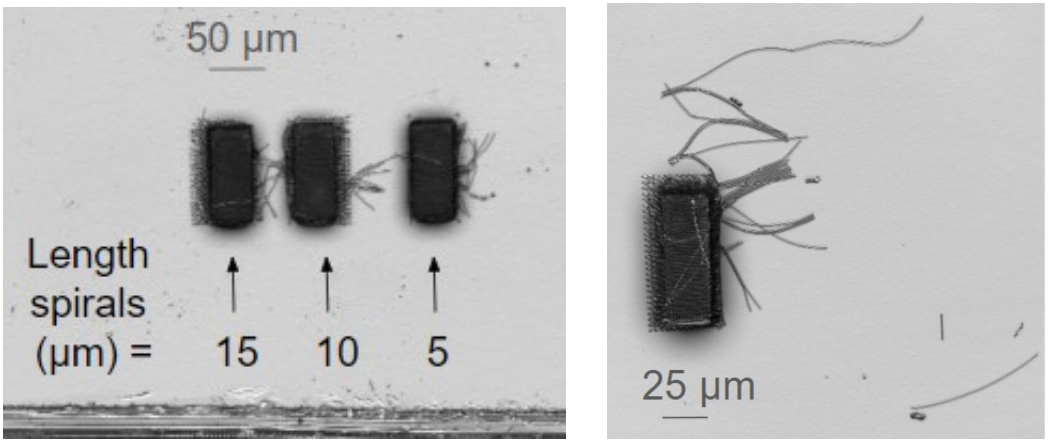

(a) **(b)**

Figure 22: Optical scanning profilometer images. (a) Chirped woodpiles of 40×90×40 µm^3 fabricated using $P = 3.25$ mW, $v = 90$ µm/s using spring-like supports of different length: 5, 10 and 15 µm. (b) Chirped woodpile of 40×90×40 µm^3 fabricated using $P = 3.25$ mW, $v = 90$ µm/s using spring-like supports of length 10 µm.

The structure that appears to be fixed better is the one on the right, which corresponds to a support's length $L_{sup} = 5 \pm 1$ µm.
An important observation worth mention is that all three structures have rods that are detached from the woodpile, as it can be easily spotted from Fig. 22a. If this imperfection is

restricted to few rods from the side, it should not represent a problem for the functionality of the photonic crystal, given that the structure consists of a big number of unit cells and a small number of defects in the edges would not have a big impact on the efficaciousness of the photonic crystal. Nevertheless, given that the spectral measurements of such small structures it's already delicate on its own, it was considered preferable to aim for structures that would not present such defects that might complicate even more their analysis.

To rule out possible sources of human error, the script used for the fabrication of the structure in Fig. 21c was used for the fabrication of a new sample, i.e. same fabrication commands, sizes, scanning velocities and powers. The resulting structure is the one shown in Fig. 22b. The expected result would have been a similar structure than the one fabricated previously (Fig. 21c), but instead, it presents once again rods detached, and in this case in larger amount.

In order to check if the problem were the supports and the first structure was just a lucky result, two sets were fabricated in the same droplet, one with supports and the other one without, each consisting of 3 woodpiles fabricated at a constant power $P = 3.25$ mW and 3 different velocities $v = 70, 80, 90$ µm/s.
This time, a part from exploring different velocities of scanning and the presence of supports, the samples were observed on the optical microscope during the whole development process (Fig. 23).

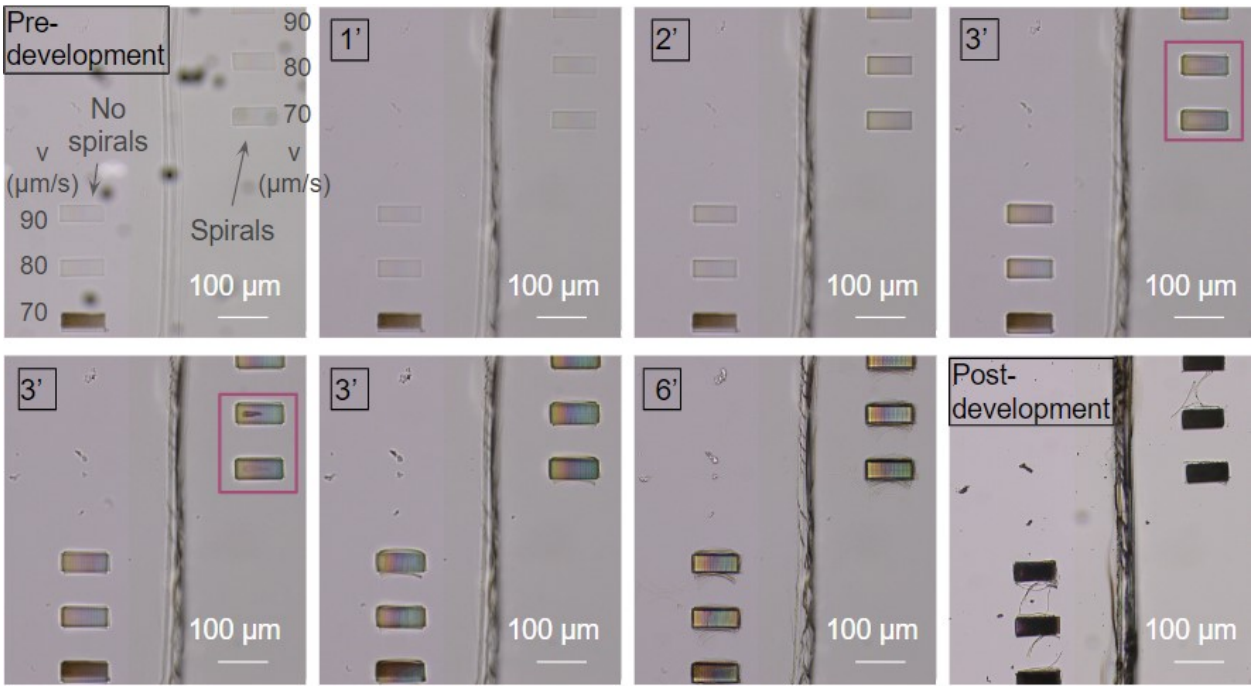

Figure 23: Optical microscope images captured during the development process. In red the structures in which it can be observed a faintly interface.

As it can be observed in the bottom-right image in Fig. 23, all the woodpiles have rods detached. When observing the evolution of the sample during the development process it's

possible to detect when the rods start to get loose, which has been done with multiple samples, and in all of them the event starts taking place 3 minutes after the developer is added. In some of them, the one being showed being an example of it (upper-right and bottom-left images in Fig. 23, regions of interest marked in red), it can be observed that the lateral rods start to detach after a faintly interface that rapidly transitions from the edges to the center disappears, like if the chemical developer was completely penetrating the woodpile, or the non-exposed resin was getting out of the inner regions.

The sample was observed using the SEM to determine from which layers the rods were detaching and to assess the degree of dismantling. The images obtained from the woodpiles fabricated with $v = 90$ µm/s with and without supports are presented in Fig. 24 as exemplification of what can be observed in all of them.

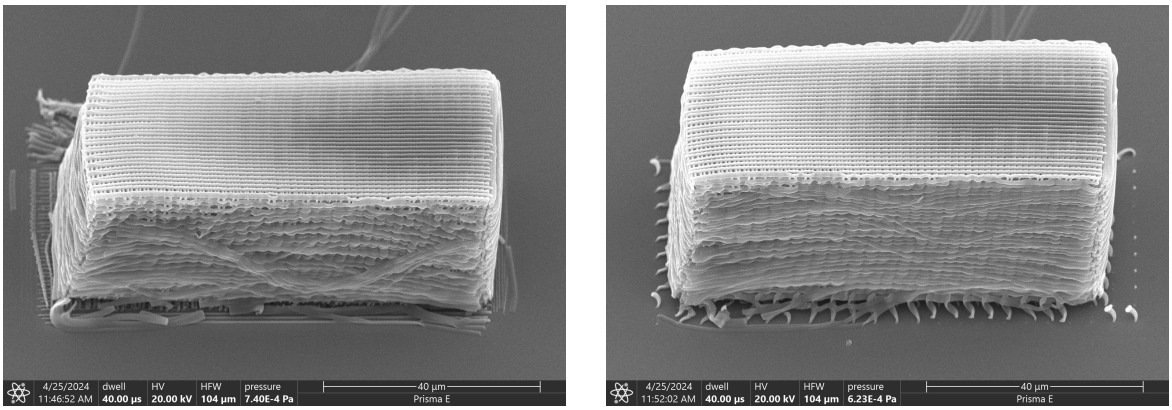

(a) **(b)**

Figure 24: SEM images of chirped woodpiles fabricated with $P = 3.25$ mW and $v = 90$ µm/s presenting rod's detachment. (a) In direct contact with the substrate. (b) With spring-like supports.

In both cases (with an without supports) the degree of detachment appears similar, and in all the layers alike. It appears that the edge rods are not always properly supported by the layer below, and they consequently fall from the woodpile, which is a strange behaviour given that the fabrication code was not modified and thus the length of the rods should be sufficient (as it was before) to support the layer above it.

The stacking distance was modified to shorten the separation between layers but the result was the same, which led to the hypothesis that it might be a problem given by the resin and not the laser writing or the structure's model.

The old SZ2080™ was used again to prepare a new batch of samples, and it was observed that the height of the droplets was higher than the one of the samples prepared with the new material even though the quantity being drop-casted and the hot-plate's temperature was the same. This was detected as soon as the material was drop-casted in the substrates, for which instead of making the whole batch with the old material, part of them samples were done using the new material and drop-casting 2 droplets once again, and some with just one droplet to check if the origin of the detachment was indeed the low height of the droplets.

The fabrication with the old SZ2080™ was not successful, but the results from the samples made from new material and two droplets were finally showing no signs of detachment, which led to the hypothesis that fabricating the structures too close to the SZ2080™-air interface, in that case due to the sample height being too short, was leading to a higher concentration of quencher[3] (oxygen acts like so in radical polymerizations) near the area being photopolymerized and thus an insufficient degree of cross-linking, leading to less robust rods and its consequent detachment.

A first fabrication of an array varying power and scanning velocity was done. After it, having an idea of which (P, v) were suitable, two pairs of woodpiles were fabricated in the same sample, using an scanning velocity $v = 60$ µm/s in all cases and, in each pair, a different power for each woodpile, one with $P = 4.00$ mW and the other $P = 3.25$ mW. The pairs were fabricated one in each side of the scratch so after fabrication they could be separated and be developed using different procedures. The half in which a part from a pair there was also the array was developed using the usual procedure of 30 minutes in 4-methyl-2-pentanone and letting it dry at room temperature, whereas the other half was left in ethanol for 2 day(s) before drying it.

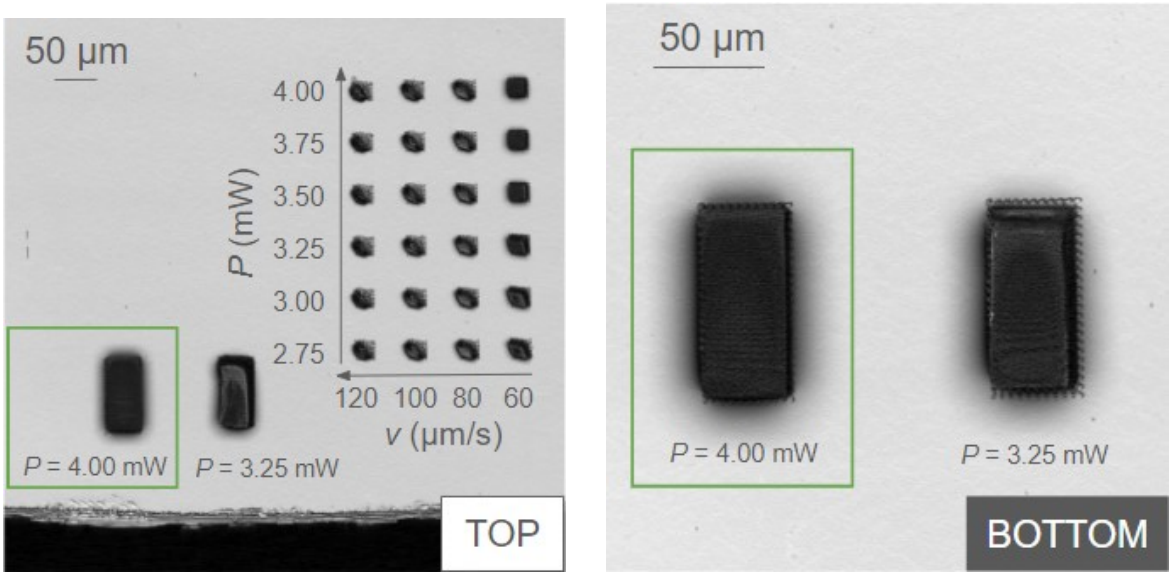

(a) **(b)**

Figure 25: Optical scanning profilometer images. (a) Developed in 4-methyl-2-pentanone for 30 minutes and immediately dried. (b) Developed in 4-methyl-2-pentanone for 30' and kept in methanol for 2 days before drying.

As it can be observed in Fig. 25, the woodpiles fabricated with the lower power ($P = 3.25$ mW) were not mechanically strong enough to maintain it's intended shape through developing, for which the study of how leaving the samples in ethanol affects the structures has been carried out focusing in the other two that do show the intended shape.

[3]molecule that suppresses the effect of propagation of the polymerization.

A bigger magnification objective was used to observe in more detail the structures fabricated using the higher power ($P = 4.00$ mW), which are presented in the following figure:

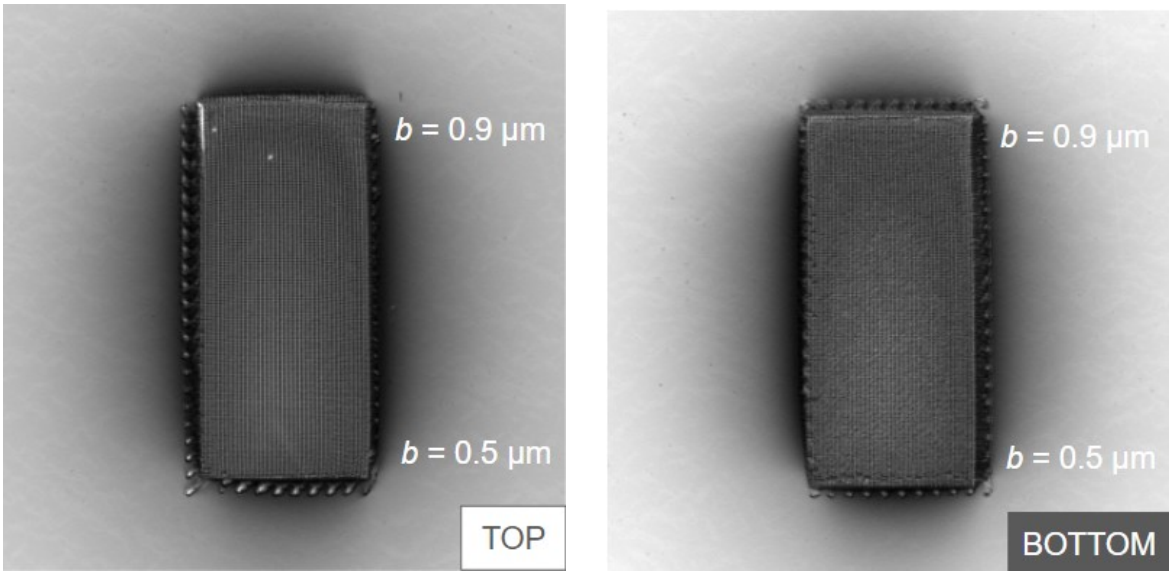

(a) **(b)**

Figure 26: Optical scanning profilometer images of woodpiles fabricated using the same parameters: $P = 4.00$ mW, $v = 60$ µm/s. (a) Developed in 4-methyl-2-pentanone for 30' and immediately dried. (b) Developed in 4-methyl-2-pentanone for 30' and kept in methanol for 2 days before drying.

As it can be observed in Fig. 26, the sample that was left in ethanol after the usual development process shows less defined rods in it's top layer, which leads to hypothesize that the material slowly degrades in ethanol.
By using the profile measurement function it has been observed that the distance between rods, as well as it's apparent height are slightly smaller in the sample left in ethanol, the biggest variation being of a 7% difference, and the smallest being null. With this information alone is not possible to determine if that treatment results in structures with a better or a worse performance as rainbow trapping photonic crystals, for which from that time on, the samples were fabricated by pairs, one in each side of the scratch, to be able to develope each copy following a different procedure.

Finally being able to fabricate once again woodpiles without defects, the design presented in Fig. 11 of 3 woodpiles with different chirping was executed with the same parameters used in the previous structures: $P = 4.00$ mW, $v = 60$ µm/s.

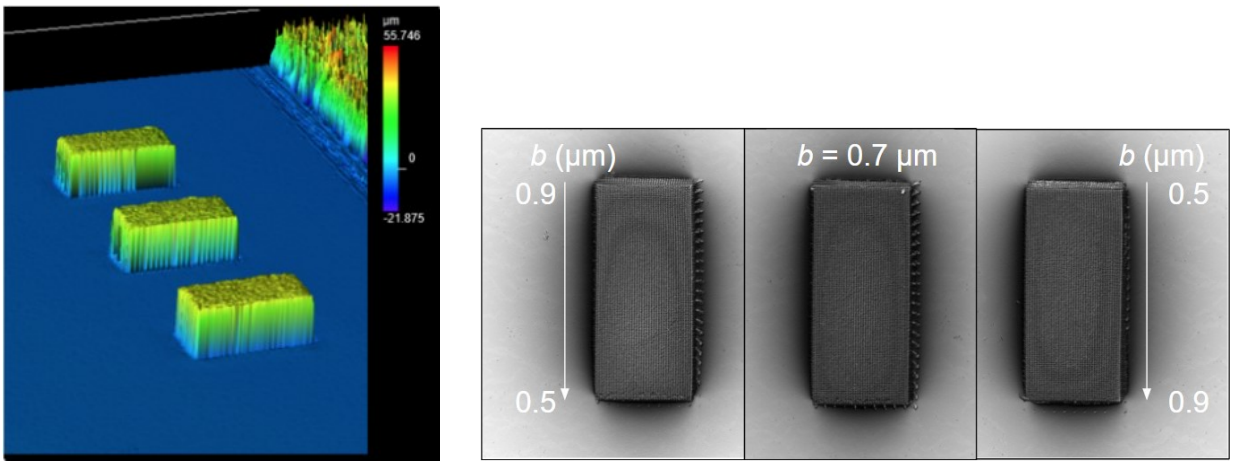

(a) (b)

Figure 27: Set of 3 woodpile structures with different chirp, fabricated using Fig. 11 design. From left to right: negative, non-, and positive chirped structures. (a) 3D scanning optical profilometer image of the surface profile in "Height mode". (b) Sscanning optical profilometer surface profile in "Intensity mode".

Sadly, just three samples were fabricated following that procedure, given that they were done as a test at last minute, after realizing that the new SZ2080™ was spreading more than the old one. The one presented in Fig. 27, as well as the other one remaining, have each one woodpile with some small part burned (attributed to the presence of dirt or bubbles present in that region), which means that comparing the results of the three different chirping on the same sample is not possible. Nevertheless, there was at least one correct woodpile of each type of chirping at some of the fabricated samples, for which they were selected as appropriate for measuring in UPC.

To continue working in that line, a new batch of samples following that sample fabrication procedure was made.Unexpectedly, the structures fabricated on that new batch showed signs of detached rods again, contradicting the hypothesis made before regarding the cause of such detachment, and it has not been possible to determine its real cause. Nevertheless, the degree of such defects did not appear to be critical for their photonic performances. In order to test if that hypothesis made on the impact of such defects was correct or not, these samples were also selected to be brought to UPC for further characterization.

4.2 Spectral Scattering Measurements

The first samples I joined the measurements of were fabricated by other researchers in the other partner university, Shizuoka University. They were first brought to Laser Research Center (LRC) where I characterized them with the optical profilometer, and I later brought them to UPC, where we finally measured them. The samples consisted in pairs of structures constituted by a positive chirped woodpile and a negative chirped one, each pair being fabricated with slightly different powers. The measurements were conducted in just one of the pairs, which was the one determined as the most promising from the images obtained with the optical profilometer, which showed no clues of deformations or defects, as seen in Fig. 29.

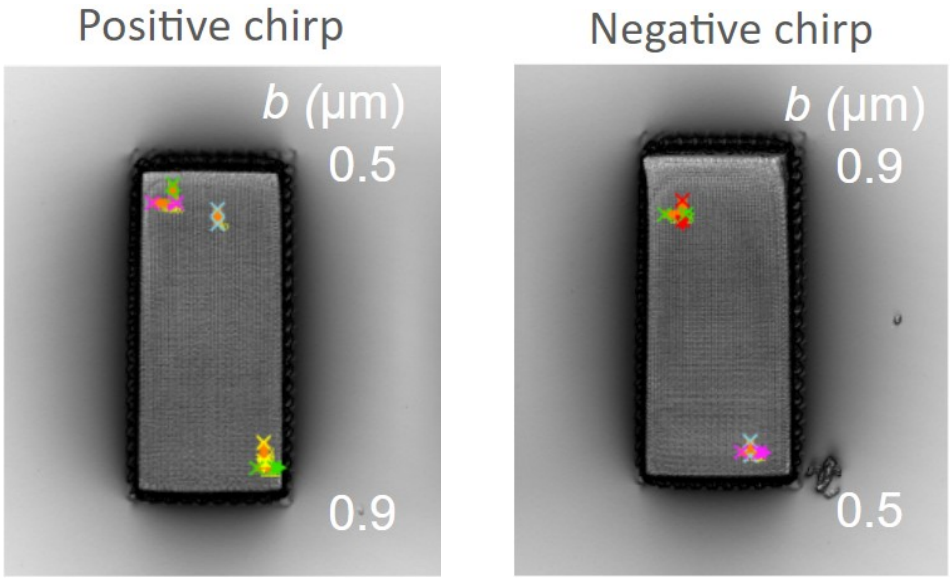

Figure 28: Structures fabricated in Shizuoka University and measured in UPC. Scanning optical profilometer images with surface profile lines used for characterization. (a) Positive chirp. (b) Negative chirp.

Later on, the selected samples fabricated in LRC were also measured, and even though it was not possible to measure them as thoroughly as the previous ones due to time constraints, and the results obtained till the moment are not as successful as the former ones, there is one interesting result worth presenting, which is the completely periodic woodpile, i.e. the structure without chirp, which was not present in the samples made in Shizuoka University. The measurements correspond to the sample presented in Fig. 27.

The corresponding results obtained in the scattering measurements are the following:

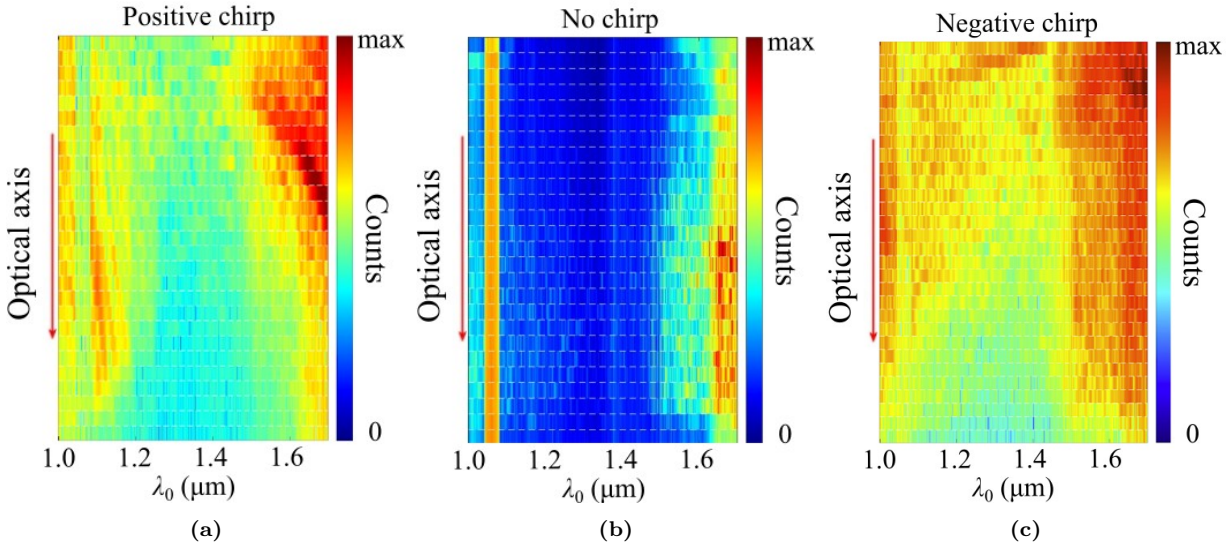

Figure 29: Experimental scattering results showing spectrally dependent light localization. (a) Positive chirp. (b) No chirp. (c) Negative chirp.

Few comments about the results will be made here, as they will be further analysed after the outcomes of the numerical simulations are presented.

First of all, an aspect worth to highlight to avoid confusions is that the wavelength $\lambda_0 = 1064$ nm is filtered out due to a peak of intensity of the super-continuum laser light at that wavelength, and it's not considered when analyzing the resulting spectra.

Secondly, the trends observed in these results are the ones expected from such structures. To begin with, the structure without chirp shows no big variations on the spectrum along the optical axis, whereas the structures with chirp clearly do. From one side, the structure with the positive chirp shows a range of wavelengths in which the intensity is lower ($\lambda_0 \approx 1.2 - 1.4$ µm), which opens up till $\lambda_0 \sim 1.6$ µm as it propagates deeper inside the crystal, and above those wavelengths, it can be observed a strong light localization that also shifts to higher wavelengths the further the light penetrates inside the crystal.
On the other side, the structure with negative chirp shows no significant difference along propagation for the longer wavelengths, but it does for the lower ones, slightly showing the inverse situation in which the localization of light, even though less intense, starts to appear for smaller wavelengths along the optical axis.

4.3 Numerical Simulations

4.3.1 Dispersion Relation, Photonic Band Diagram and Group Velocities

The structure has the symmetry of a body-centered orthorhombic lattice as it's depicted in Fig. 30, which can be described by the lattice vectors $\{\mathbf{a}_1, \mathbf{a}_2, \mathbf{a}_3\}$ specified in Eq. (27) and reciprocal lattice vectors $\{\mathbf{b}_1, \mathbf{b}_2, \mathbf{b}_3\}$ specified in Eq. (28).

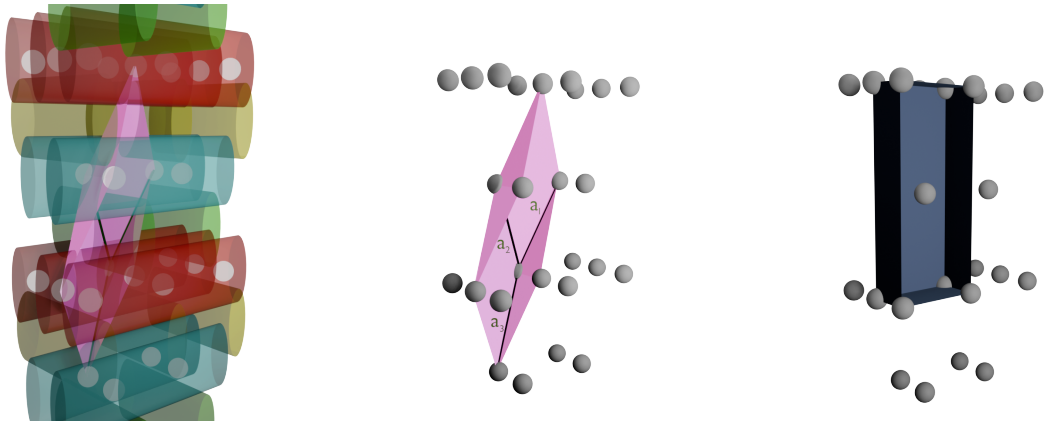

(a) **(b)** **(c)**

Figure 30: (a) Structure with lattice points, vectors and unit cell. (b) Body-Centered Orthorhombic primitive unit cell. (c) Body-Centered Orthorhombic unit cell.

$$\mathbf{a}_1 = \frac{1}{2}(-a, b, c), \qquad \mathbf{a}_2 = \frac{1}{2}(a, -b, c), \qquad \mathbf{a}_3 = \frac{1}{2}(a, b, -c) \tag{27}$$

$$\mathbf{b}_1 = 2\pi\left(0, \frac{1}{b}, \frac{1}{c}\right), \qquad \mathbf{b}_2 = 2\pi\left(\frac{1}{a}, 0, \frac{1}{c}\right), \qquad \mathbf{b}_3 = 2\pi\left(\frac{1}{a}, \frac{1}{b}, 0\right) \tag{28}$$

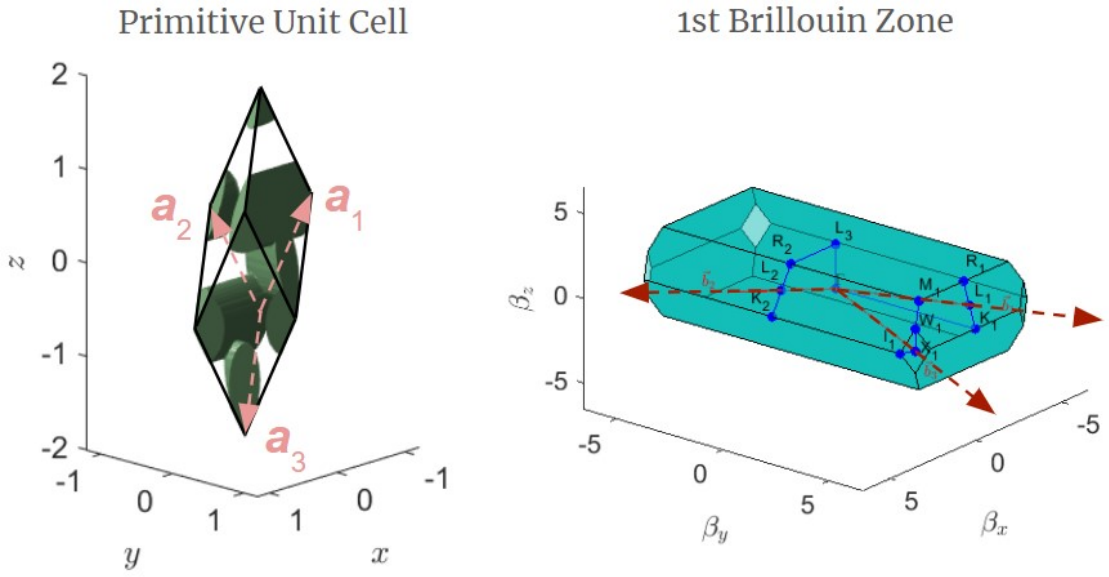

Figure 31: Primitive unit cell and 1st Brillouin zone of the structure with the corresponding lattice vectors. The blue points connected through a blue line correspond to the high symmetry points and the path followed along the limits of the 1BZ used to generate the photonic band diagram.

The graphical representation of the primitive unit cell as well as its corresponding 1BZ has been extracted from the code in which the photonic band diagram is simulated (Fig. 31). The symmetry points used to scan the reciprocal space and generate the photonic band diagram are shown in blue, and the corresponding coordinates are defined in terms of the reciprocal lattice vectors and other symmetry points as shown in Eq. (29).

Symmetry points:

$$
\begin{aligned}
&\Gamma\text{: } (0,\,0,\,0) && \text{M}_1\text{: } R_2 + R_1 - L_3 && \text{K}_2\text{: } \tfrac{1}{4}\left(1+\tfrac{a^2}{c^2}\right)(-2\mathbf{b}_1+\mathbf{b}_2+\mathbf{b}_3)\\
&\text{K}_1\text{: } \tfrac{1}{4}\left(1+\tfrac{b^2}{c^2}\right)(\mathbf{b}_1-\mathbf{b}_2+\mathbf{b}_3) && \text{W}_1\text{: } \tfrac{1}{4}(\mathbf{b}_1+\mathbf{b}_2+\mathbf{b}_3) && \text{L}_2 : \frac{1}{2}\mathbf{b}_2 = \pi\left(\frac{1}{a},\frac{1}{b},0\right)\\
&\text{L}_1\text{: } \tfrac{1}{2}\mathbf{b}_1 = \pi\left(0,\tfrac{1}{b},\tfrac{1}{c}\right) && \text{X}_1\text{: } \tfrac{1}{2}\mathbf{b}_3 = \pi\left(\tfrac{1}{a},0,\tfrac{1}{c}\right) && \text{R}_2\text{: } 2\cdot L_2 - K_2\\
&\text{R}_1\text{: } 2\cdot L_1 - K_1 && \text{I}_1\text{: } K_2 + R_1 - L_3 && \text{L}_3\text{: } \tfrac{1}{2}(\mathbf{b}_1+\mathbf{b}_2-\mathbf{b}_3)
\end{aligned}
\tag{29}
$$

The photonic band diagrams for the smallest and largest lattice constant are shown in the following figure (Fig. 32):

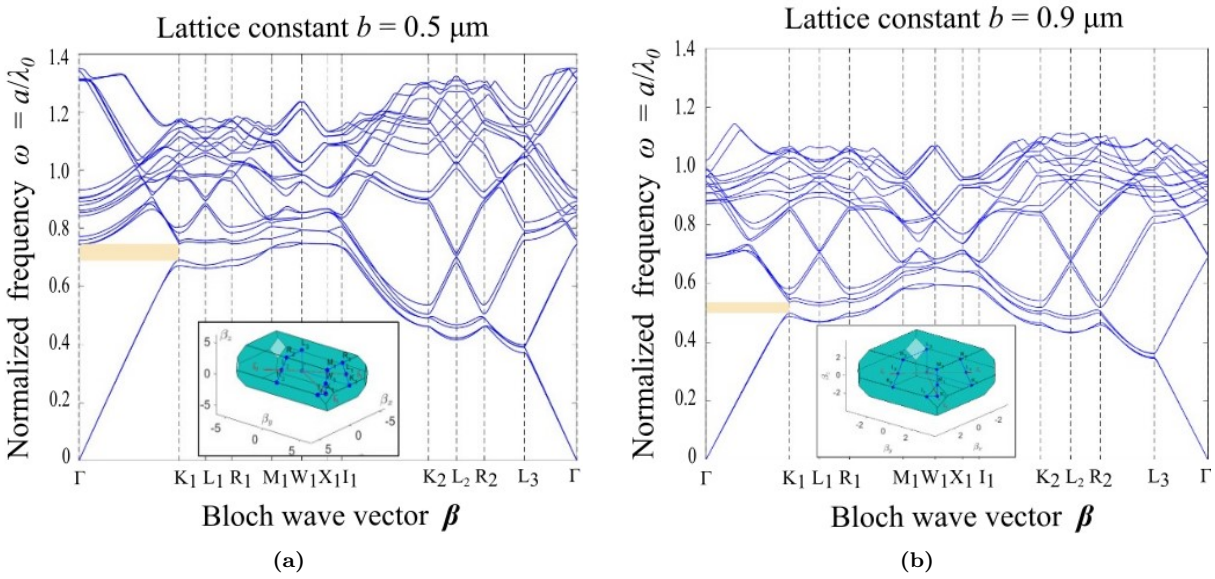

Figure 32: Photonic band diagrams corresponding to the completely 3D periodic structure with (a) Small lattice constant $b = 0.5$ µm. (b) Big lattice constant $b = 0.9$ µm. The rest of the lattice constants are kept unchanged $a = 0.$ µm and $c =$ µm. The insets in each graph are the corresponding Brillouin zones.

As it can be seen, a complete band-gap is not present in any of the cases, but for the angle of incidence at which the laser beam was planned to be focused (corresponding to a wavevector along the direction $\overrightarrow{\Gamma K_1}$), a band gap opens above the second band, and the band flattens near that edge of the 1BZ.

In order to assess how the band gap evolves as the lattice constant changes, i.e. throughout the crystal, the corresponding wavelengths at which it appears for each lattice constant b are plotted as a function of this parameter, Fig. 33a, which gives a direct idea of how deep inside the crystal each wavelength will propagate before encountering the band gap.

In a similar way, the evolution of the group velocity of a specific wavelength has been also calculated and represented in a graph, Fig. 33b. The wavelength of choice, $\lambda_0 = 1.6$ µm has been taken as an example of wavelength that encounters the band gap after propagating a certain depth inside the crystal, which should offer a broader view of how the group velocity is affected as it propagates inside a woodpile photonic crystal with a chirp.

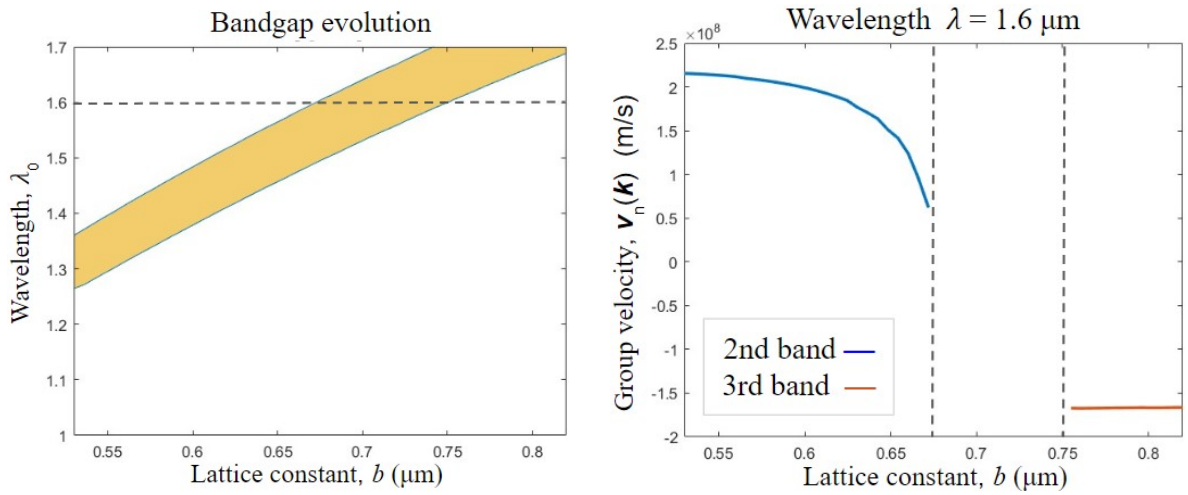

(a) **(b)**

Figure 33: (a) band-gap evolution as funtion of the lattice constant b. (b) Group velocity as function of lattice constant b for the wavelength $\lambda_0 = 1.6$ μm. The blue line corresponds to the group velocity of $\lambda_0 = 1.6$ μm while is found in the second band, whereas the red corresponds to when it's in the third band, above the band gap. The blank space between them corresponds to the band-gap.

The range of b for which this plot has been done corresponds to the range of lattice constants estimated from the profilometer measurements for the sample presented in Fig. 27, which has been used to exemplify the general trend, and the range of wavelengths corresponds to that at which the scattering measurements will be taken.

As it can be seen in the first figure, Fig. 33a, the resulting band gap appears for longer wavelengths as the lattice constant increases, starting approximately for the range 1.26 – 1.36 μm at the entrance of the crystal, and finishing above the measurable limit. From this results, the expected behaviour is that the wavelengths corresponding to the initial band gap don't even enter the crystal, while the ones above it will couple inside the woodpile but it's propagation will stop at the point at which the band gap is encountered.

By taking then a look at the results of the group velocity, the first thing to observe is that the velocity is first positive and decays almost following a negative exponential $\sim -e^z$ before disappearing, which corresponds to the region in which it has the band gap, and after that, the velocity appears to be negative and constant, which corresponds to when that wavelength is found in the third band.
What can be deduce from this results is that this wavelength component will, as it was theorized, slow down as it gets closer to the band gap, after which its propagation inside the crystal is forbidden, for which is not expected to have such component after it reaches the band gap.

4.3.2 Reflection and Transmission

The simulations have been done again for a chirped woodpile with the structural parameters estimated from the optical profilometer measurements, and covering the range of frequencies

that are measured in the spectral scattering measurements $\lambda_0 = 1.0 - 1.7$ µm.

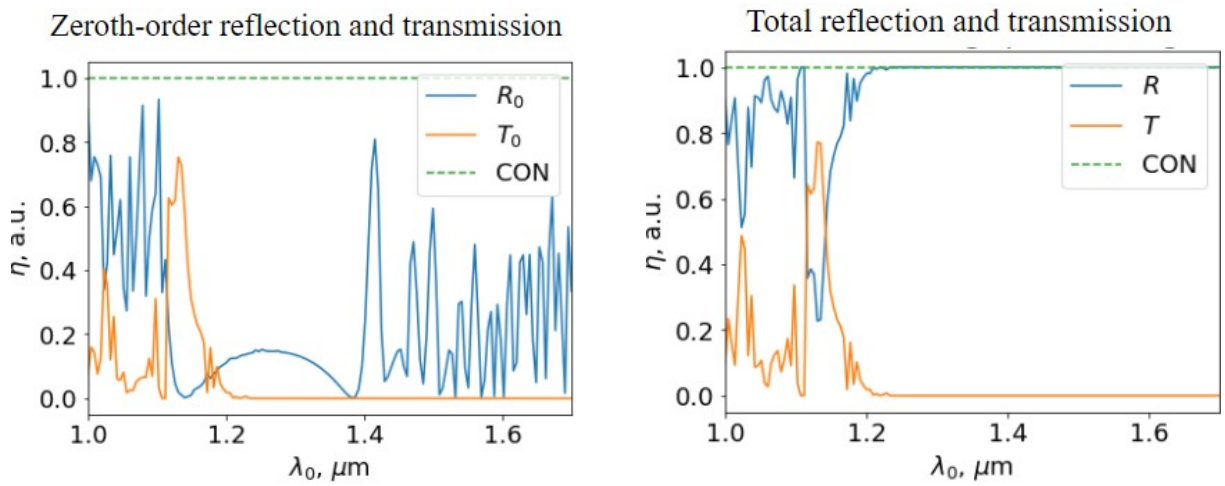

(a) (b)

Figure 34: Reflection and transmission curves obtained from RCWA simulation.(a) Zeroth-order R and T. (b) Total R and T.

The resulting plot, Fig. 34a shows the zeroth order reflection and transmission of the structure for normal incidence. As it can be observed, the transmission of the zeroth order drops down to zero around $\lambda_0 \approx 1.2$ µm, whereas the zeroth reflection appears to be lower in the range $\lambda_0 \approx 1.15 - 1.4$ µm, but it shows peaks and valleys in the rest of the spectra under analysis. As it can be seen in the plot of the total reflection and transmission, i.e. accounting for the different orders, the transmission curve appear to be almost identical, meaning that light gets transmitted in the zeroth order, but as it can be observed, light above $\lambda_0 \approx 1.2$ µm gets fully reflected, matching the range of wavelengths that will encounter the band-gap condition at some point through the crystal, only difference is that big part of it is in other diffraction orders.

This simulation needs to be further improved and optimized, nevertheless, it's something that has been left as future work, given that the results can not be yet compared with experimental measurements due to the current setup not being prepared for acquiring such data.

4.3.3 Electric Field Propagation

Finally, the results obtained with the last simulation method are presented in Fig. 35, which are the most useful ones to compare with the scattering measurements. The three chirp cases, i.e. positive, null and negative, have been simulated, and clear differences can be spotted between them.

The region in which attention has been focused is the one above $\lambda_0 = 1.2$ µm, which is the one that corresponds to the wavelenghts at which the band gap between the second bands and the ones right above it is found, as presented in the band diagrams (Fig 4). As

expected, the photonic crystal with positive chirp shows initially no presence of wavelength components in the range $\lambda_0 \approx 1.25 - 1.4$ µm, which opens as going further inside the crystal, ending up with no wavelength components in $\lambda_0 \approx 1.2 - 1.7$ µm, and an increase of intensity where the light stops propagating, as expected. For the negative chirp an analogous behaviour is observed, but in this case the initial band gap is found for the higher range of wavelengths $\lambda_0 \approx 1.6 - 1.7$ µm and it opens till $\lambda_0 \approx 1.2 - 1.7$.

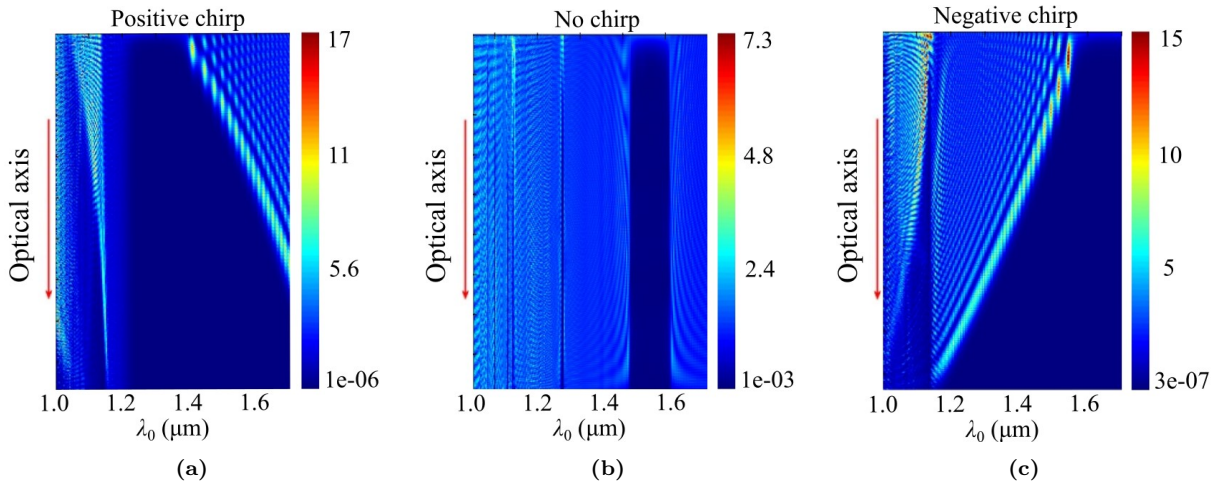

Figure 35: FDTD simulation of Re(E) field propagation. (a) Positive chirp. (b) Without chirp. (c) Negative chirp.

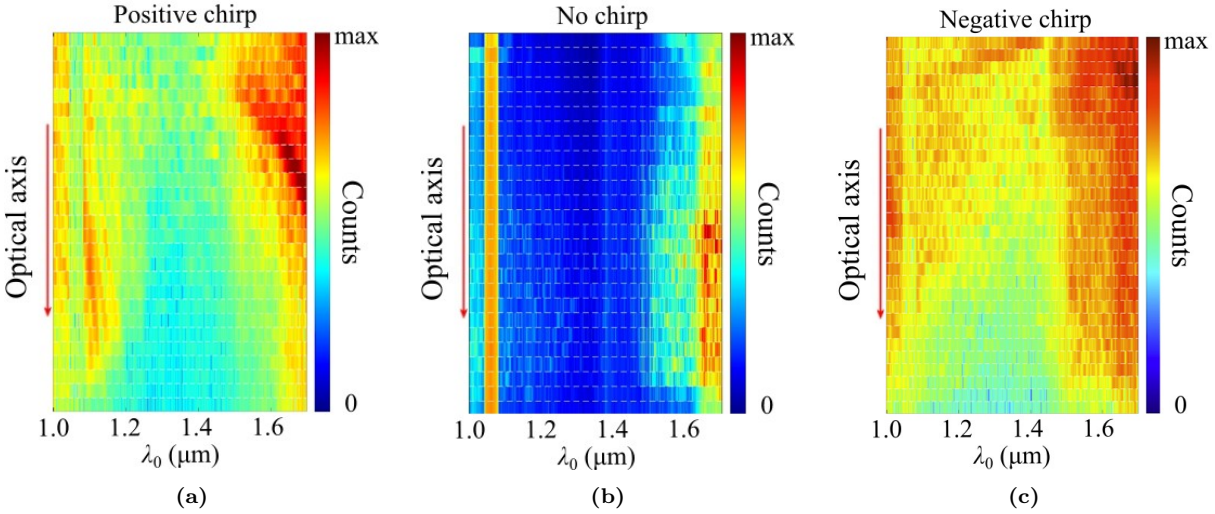

Figure 36: Experimental scattering results. (a) Positive chirp. (b) Without chirp. (c) Negative chirp.

When comparing the theoretical results with the experimental ones, they do not show 100% of agreement but they do present the same trends. The deviations can be attributed to the uncertainty of the structure parameters, as well as inaccuracies inherent in the measuring process, both of which could be further amended and steps are being taken towards that direction. Nonetheless, the results have been considered to come up to a sufficient degree of agreement to consider this experiment successful.

5 Main Results

From the study of the fabrication and design parameters, it has been determined that:

- An **increase in P**, and thus an **increase in I** results in **less shrinkage**, whereas an **increase in v** results in **more shrinkage**.
- The **dynamic fabrication range**, has been found to be **varying** from sample to sample, being the **optimal dynamic fabrication range** around $P = 3$ – 4 mW, corresponding to an intensity $I = 0.43$ – 0.58 TW/cm^2, and $v = 50$ – 100 µm/s.
- The implementation of **spring-like supports** solved the problem of **non-uniform shrinkage** of the structures by avoiding having them in direct contact with the substrate.

From the spectral scattering measurements it has been observed that:

- **Frequency dependent light localization** is **present** in the **3D chirped woodpile structures**, showing this enhancement towards shorter or longer wavelengths depending on the evolution of the lattice constant.

From the numerical simulations it has been observed that:

- A **band-gap** is **present in the NIR range**, and it **evolves** from shorter to longer wavelengths when the lattice constant b is increased, and the other way around for the opposite situation.
- The **group velocity** of a certain wavelength component **decreases** when **approaching the band gap** condition.
- The structure appears to **fully reflect** those wavelengths which encounter the **band-gap condition** at some position along the crystal.
- The propagation of electromagnetic fields through such structures presents signs of **spatial spectral localization** when implementing a **chirp in the lattice constant** tangential to the propagation direction.

6 Conclusions

1. Spectral light localization arises in 3D gradient PhCs from the combination of small group velocity near the band-gap and the adiabatic variation of the local dispersion relation, concluded from the correlation found between the increase of intensity homogeneously varying along the propagation, and the decrease of the group velocity near the band-gap and its dependence on the lattice constant obtained in the numerical simulations.

2. It has been empirically determined that the optimal parameters for the fabrication of 3D sub-micron lateral gradient woodpiles with rod widths of $d_{xy} \approx 300$ nm are: $NA = 1.4$, $I = 0.43$ – 0.58 TW/cm^2 and $v =$ 50 – 100 µm/s.

3. Spectral light localization in the NIR range $\lambda_0 = 1.0$ – 1.7 µm was observed by the scattering of the 3D gradient structures when focusing a super-continuum laser beam in them.

4. 3D gradient woodpiles PhC fabricated via TPL are featuring slow light and spectral localization in the NIR regime, the experimental results being in agreement with the numerical simulations.

7 Future work

- Design a new experiment to further study what is the cause of the detachment of rods encountered in most of the fabricated woodpiles.
- Implement other developing or post-developing techniques such as Critical Point Drying or calcination to study the possibility of scaling down to the visible range the light localization effect.
- Improve the RCWA simulations and test out the results once the experimental setup is upgraded to perform the corresponding measurements.

8 References

[1] H Kodama. Automatic method for fabricating a three-dimensional plastic model with photo-hardening polymer. Review of Scientific Instruments, 52(11):1770–1773, 1981.

[2] J. Huang, Q. Qin, and J. Wang. A review of stereolithography: Processes and systems. Processes, 8(9), 2020.

[3] En S. Wu, James H. Strickler, William R. Harrell, and Watt W. Webb. Two-photon lithography for microelectronic application. In Advanced Lithography, 1992.

[4] O. Nakamura S. Maruo and S. Kawata. Three-dimensional microfabrication with two-photon-absorbed photopolymerization. Opt. Lett., 22(2):132–134, 1997.

[5] S. Thiele A. Herkommer M. Schmid, F. Sterl and H. Giessen. 3D printed hybrid refractive/diffractive achromat and apochromat for the visible wavelength range. Opt. Lett., 46(10):2485–2488, 2021.

[6] J. Lölsberg, J. Linkhorst, A. Cinar, A.r Jans, A. Kuehne, and M. Wessling. 3D nanofabrication inside rapid prototyped microfluidic channels showcased by wet-spinning of single micrometre fibres. Lab Chip, 18:1341–1348, 2018.

[7] A. Accardo et al. Multiphoton direct laser writing and 3D imaging of polymeric freestanding architectures for cell colonization. Small, 13(27):1700621, 2017.

[8] M. Turner et al. Miniature chiral beamsplitter based on gyroid photonic crystals. Nature Photon, 7:801–805, 2013.

[9] E. Yablonovitch. Inhibited spontaneous emission in solid-state physics and electronics. Phys. Rev. Lett., 58:2059–2062, May 1987.

[10] E. Cubukcu, K. Aydin, E. Ozbay, S. Foteinopoulou, and C. M. Soukoulis. Negative refraction by photonic crystals. Nature, (423):604–605, 2003.

[11] K. Inoue, N. Kawai, Y. Sugimoto, N. Carlsson, N. Ikeda, and K. Asakawa. Observation of small group velocity in two-dimensional algaas-based photonic crystal slabs. Phys. Rev. B, 65:121308, 2002.

[12] D. Biallo, A. D'Orazio, M. Sario, V. Marrocco, V. Petruzzelli, and F. Prudenzano. Photonic crystal sensors. volume 2, pages 44 – 48, 07 2006.

[13] E. Glushko, V. N. Evteev, and A. Stepanyuk. All-optical signal processing in photonic crystals covered with fast nonlinear materials. Proc SPIE, 6889, 2008.

[14] Lina Maigyte and Kestutis Staliunas. Spatial filtering with photonic crystals. Appl. Phys. Rev., 2:011102, 02 2015. doi: 10.1063/1.4907345.

[15] J. C. Knight, T. A. Birks, P. St. J. Russell, and D. M. Atkin. All-silica single-mode optical fiber with photonic crystal cladding. Opt. Lett., 21(19):1547–1549, 1996.

[16] R. Phillips. Photopolymerization. Journal of Photochemistry, 25(1):79–82, 1984.

[17] G. Odian. Principles of Polymerization. Wiley-Blackwell, 2004.

[18] E. Skliutas, M. Lebedevaite, E. Kabouraki, T. Baldacchini, J. Ostrauskaite, M. Vamvakaki, M. Farsari, S. Juodkazis, and M. Malinauskas. Polymerization mechanisms initiated by spatio-temporally confined light. Nanophotonics, 10(4):1211–1242, 2021.

[19] M Malinauskas, A. Žukauskas, G. Bičkauskaitė, R. Gadonas, and S. Juodkazis. Mechanisms of three-dimensional structuring of photo-polymers by tightly focussed femtosecond laser pulses. Opt. Express, 18(10):10209–10221, 2010.

[20] A. Žukauskas, G. Batavičiūtė, M. Ščiuka, Z. Balevičius, A. Melninkaitis, and M. Malinauskas. Effect of the photoinitiator presence and exposure conditions on laser-induced damage threshold of ORMOSIL (SZ2080). Opt. Mater., 39:224–231, 2015.

[21] M. Malinauskas and Kiršanskė et al. Nanophotonic lithography: a versatile tool for manufacturing functional three-dimensional micro-/nano-objects. Lith. J. Phys., 52: 312–326, 2012.

[22] H. Wang et al. Two-photon polymerization lithography for optics and photonics: Fundamentals, materials, technologies, and applications. Adv. Funct. Mater., 03 2023.

[23] S. Varapnickas and M. Malinauskas. Processes of Laser Direct Writing 3D Nanolithography. Springer International Publishing, 2020.

[24] S. Dengler and B. Eberle. Investigations on the nonlinear optical properties of 0D, 1D, and 2D boron nitride nanomaterials in the visible spectral region. Nanomaterials, 13: 1849, 2023.

[25] Fabrication of 3D polymeric microstructures using pulsed 3D direct laser lithography. Technical report, Vilnius University, Faculty of Physics, Laser Research Center, 2021.

[26] K. Wang and Z. Wang. Shrinkage stress evolution during photopolymerization: Theory and experiments. J Mech Phys Solids, 178:105350, 2023.

[27] E. Yablonovitch. Photonic crystals : What's in a name? Opt Photonics News, 18: 12–13, 2007.

[28] P. Viktorovitch et al. Photonic crystals: basic concepts and devices. C R Phys, 8(2): 253–266, 2007. Recent advances in crystal optics.

[29] C. M. Soukoulis. The history and a review of the modelling and fabrication of photonic crystals. Nanotechnology, 13(3):420, 2002.

[30] E. Yablonovitch and T. J. Gmitte. Photonic band structure: The face-centered-cubic case. Phys. Rev. Lett., 63:1950–1953, Oct 1989.

[31] S. Olyaee and A. Naraghi. Chapter 23 - recent progress in therapeutic diagnosis using photonic crystal nanostructures. In Nanostructures for Novel Therapy, Micro and Nano Technologies, pages 621–656. Elsevier, 2017.

[32] Chapter 1. photonic crystals: properties and application. URL `https://ses.library.usyd.edu.au/bitstream/handle/2123/924/02whole.pdf`.

[33] J. Sajeev. Strong localization of photons in certain disordered dielectric superlattices. Phys. Rev. Lett., 58:2486–2489, 1987.

[34] Lord Rayleigh. Xvii. on the maintenance of vibrations by forces of double frequency, and on the propagation of waves through a medium endowed with a periodic structure. Lond. Edinb. Dublin philos. mag. j. sci., 24(147):145–159, 1887.

[35] S. G. Johnson. Introduction to photonic crystals: Bloch's theorem, band diagrams, and gaps (but no defects). 2003.

[36] J. D. Joannopoulos, S. G. Johnson, J. N. Winn, and R. D. Meade. Photonic Crystals: Molding the Flow of Light. Princeton University Press, 1995.

[37] H. Liu, J. Yao, D. Xu, and P. Wang. Characteristics of photonic band gaps in woodpile three-dimensional terahertz photonic crystals. Opt. Express, 15:695, 2007.

[38] L. Ibbotson, A. Demetriadou, S. Croxall, O. Hess, and J. Baumberg. Optical nano-woodpiles: Large-area metallic photonic crystals and metamaterials. Sci. Rep., 5:8313, 2015.

[39] Z. Hayran, H. Kurt, and K. Staliunas. Rainbow trapping in a chirped three-dimensional photonic crystal. Sci. Rep., 7, 2017.

[40] D. Ladika et al. X-photon 3D lithography by fs-oscillators: wavelength-independent and photoinitiator-free. Res. Sq., 2023.

9 Acknowledgments

Firstly, I would like to thank Prof. Mangirdas Malinauskas for the opportunity that was given to me. It has been a challenging and enriching experience that opened to me a branch of research on photonics that I did not know of. I would like to thank as well the encouragment, support and the trust given through all the year.

Secondly, I want to express my gratitude to Dr. Darius Gailevičius and PhD student Ignas Lukošiūnas for all the help, all the time they dedicated to help me, for all what I have learned from both, and for the time spent together, and thank Dr. Donatas Narbutis for his help on the characterization of the structures.

I would also like to sincerely thank the UPC's DONLL group, specially Prof. Crina Cojocaru and Prof. Jose Trull for hosting me and making me feel like part of the group since the first day, and to PhD student Eva Otero Picón and MS student Bertran Soria Pastor, from whom I learned and with whom I spent all the time of my visit in UPC.

Next, I would like to thank all the people in LRC, who made me feel welcomed and in a pleasant working environment, and specially to the head of the department Dr. Dalia Kaškelytė for the support given.

Finally, I would like to thank all my family, friends and my boyfriend for all the support given even though the distance barrier, and for being encouraging and understanding the whole time.

Fabrication and characterization of 3D gradient photonic structures via laser lithography

Eulàlia Puig Vilardell

Two-Photon Lithography technique (TPL) has attracted a lot of attention given the ability to fabricate complex 3D micro- and nano-structures with high-precision and sub-diffraction-limit resolution. This trait makes it be a favourable technique to fabricate complex 3D photonic crystals (PhC), which is another area of high interest in the photonic's field nowadays.

The aim of this work is to fabricate using this technique a 3D gradient PhC able to slow down and spectrally localize the light in the near infrared regimes, which could be applied for sensing given the fact that an increase of intensity enhances light-matter interactions.

To begin with, an introduction of the work is provided in the first section. The review of some of the literature found on both the fabrication technique and on photonic crystal is presented next in Section 2.
The description of the experimental methods follows up in Section 3, in which the general workflow that is followed for the fabrication and characterization of the structures is first described, after which the different experiments designed for each task are presented, and finally the principles and formulation of the numerical simulations are introduced.
In Section 4, all the results are presented and discussed, covering from the fabrication process, the characterization and scattering measurements, up to the numerical results, in the mentioned order. The results regarding the fabrication of the structures and the challenges and difficulties faced during the process is the most extended one, being the main part of this study, whereas the scattering measurements correspond just to those few done in the course of this work, leaving out of this thesis the results obtained previously in the frame of the project collaboration.

Finally, the main results and conclusions derived from the study are summarized in the last sections, were is concluded that 3D PhC able to slow down and spectrally localize light in the NIR regime can be fabricated via TPL, the effect of which has measured and found in accordance with the theoretical predictions obtained with the numerical simulations.

Fabricació i caracterització d'estructures fotòniques 3D amb gradient via litografia laser

Eulàlia Puig Vilardell

La tècnica de litografia de dos fotons (LDF) ha atret gran atenció donada l'habilitat de fabricar micro- i nano- estructures 3D complexes amb gran precisió i amb resolucions per sota el límit de difracció. Aquest tret la converteix en una tècnica favorable per la fabricació de cristalls fotònics (CF) 3D complexos, els quals constitueixen una altra àrea d'alt interès actualment en el camp de la fotònica.

L'objectiu d'aquest treball és fabricar utilitzant aquesta tècnica un CP 3D amb gradient capaç d'alentir i localitzar espectralment la llum de la regió de l'infraroig proper, el qual podria tenir aplicacions en sensors, tenint en compte que un increment d'intensitat potencia les interaccions llum-matèria.

Per començar, una introducció del treball es proporciona a la primera secció. Una ressenya bibliogràfica tant sobre la tècnica de fabricació com sobre els CF és presentada seguidament a la Secció 2.
La descripció dels mètodes experimentals apareix tot seguit a la Secció 3, en la qual el procediment de treball general que es segueix per dur a terme la fabricació i caracterització de les estructures és primerament descrit, després del qual els diferents experiments dissenyats per cada tasca són presentats, i finalment els principis i la formulació de les simulacions numèriques són introduïdes.
A la Secció 4, es presenten tots els resultats i se'n fa una discussió, cobrint des del procés de fabricació, la caracterització i les mesures de dispersió, fins als resultats numèrics, en l'ordre mencionat. Els resultats més extensos són els de la fabricació de les estructures i els reptes i dificultats trobades durant el procés, ja que corresponen a la part principal de l'estudi, mentre que les mesures de dispersió presentades són només aquelles fetes durant el transcurs d'aquest treball, deixant fora d'aquesta tesis els resultats obtinguts prèviament en el marc de la col·laboració del projecte.

Finalment, els resultats principals i les conclusions extretes de l'estudi són sintetitzades en les últimes seccions, on es conclou que CFs 3D capaços d'alentir i localitzar espectralment la llum de la regió de l'infraroig poden ser fabricats via LDF, efecte el qual ha sigut mesurat i ha resultat trobar-se en concordància amb les prediccions teòriques obtingudes amb les simulacions numèriques.